RESEARCH ARTICLE | OCTOBER 15 2024

Mitigation mechanism of porous media hood for the sonic boom emitted from maglev tunnel portals

Special Collection: Flow and Civil Structures

Kai-Wen Wang (王凯文) ; Guang Chen (陈光) ; Chih-Yung Wen (温志湧) ; Xiao-Hui Xiong (熊小慧) ; Xi-Feng Liang (梁习锋) ; Lei Zhang (张雷)

Physics of Fluids 36, 106134 (2024)
https://doi.org/10.1063/5.0231438

Physics of Fluids ARTICLE pubs.aip.org/aip/pof

Mitigation mechanism of porous media hood for the sonic boom emitted from maglev tunnel portals

Cite as: Phys. Fluids **36**, 106134 (2024); doi: 10.1063/5.0231438
Submitted: 31 July 2024 · Accepted: 18 September 2024 ·
Published Online: 15 October 2024

Kai-Wen Wang (王凯文),[1,2,3] Guang Chen (陈光),[1,2,3] Chih-Yung Wen (溫志湧),[4] Xiao-Hui Xiong (熊小慧),[1,2,3,a)] Xi-Feng Liang (梁习锋),[1,2,3] and Lei Zhang (张雷)[1,2,3]

AFFILIATIONS

[1]Key Laboratory of Traffic Safety on Track of Ministry of Education, School of Traffic & Transportation Engineering, Central South University, Changsha 410075, China
[2]Joint International Research Laboratory of Key Technology for Rail Traffic Safety, Central South University, Changsha 410075, China
[3]National & Local Joint Engineering Research Center of Safety Technology for Rail Vehicle, Central South University, Changsha 410075, China
[4]Department of Aeronautical and Aviation Engineering, The Hong Kong Polytechnic University, Kowloon, Hong Kong, China

Note: This paper is part of the special topic, Flow and Civil Structures.
[a)]**Author to whom correspondence should be addressed:** xhxiong@csu.edu.cn

ABSTRACT

The micro-pressure waves (MPW) released from maglev tunnel portals can generate audible sonic booms and cause structural resonance in surrounding buildings, posing challenges to developing high-speed maglev trains. This paper proposes a novel porous media hood (PMH) and investigates its mechanism for mitigating the sonic booms emitted from tunnels. The numerical model employs the improved delayed detached eddy simulation turbulence model and overset grid technology, validated against data from moving-model experiments. The influences of the PMH's inherent properties and geometric parameters on MPW, flow field evolution, and aerodynamic loads on the train body were comprehensively discussed. The research demonstrates that PMH effectively dampens the initial wavefront gradient at the entrance and reduces the MPW amplitude by intensifying radiation within its exit vicinity. The porosity of 0.2 facilitates a seamless transition for the streamlined head from the ventilated PMH to the airtight tunnel. Lengthening the PMH enhances its MPW mitigation effect, whereas the impact of PMH thickness is minor. The PMH effectively diminishes the reflection intensity of compression and expansion waves at the tunnel ends, leading to a reduction in the magnitude and changing rate of train aerodynamic loads. This underscores the PMH's potential to enhance passengers' auditory comfort and alleviate issues related to train sway.

I. INTRODUCTION

High-speed maglev trains have emerged as the cutting-edge direction in transportation development, leveraging their advantages of low noise, high energy efficiency, and exceptional speed.[1] The maximum operating speed of the Shanghai Maglev Line has reached 430 km/h.[2] The maximum speeds of the next-generation high-speed maglev trains released by Japan and China are 603 and 600 km/h, respectively.[3,4] However, the transition of maglev trains from commercial operation at 430 to 600 km/h faces a multitude of challenges, notably those about their aerodynamics.

The coupled train/tunnel aerodynamic effect has garnered significant attention from scholars.[5] The compression waves and expansion waves caused by the entry of the train's head and tail into the tunnel will continue to propagate and superimpose within the tunnel. When the initial wavefront reaches the tunnel exit, part radiates as low-frequency micro-pressure waves (MPW),[6] and the MPW amplitude is proportional to the wavefront gradient amplitude at the tunnel exit.[7] When the train speed increases from 400 to 600 km/h, the aerodynamic effects within the tunnel will pose a threat to the structural strength of the train body, auxiliary facilities within the tunnel, and human ear comfort.[8] For instance, within the speed range of 400–600 km/h, the positive pressure amplitudes on the train surface and tunnel wall are proportional to the 2.3th and 2.46th powers of the train speed, respectively, exceeding the power exponents of 2.04 and 2.15

observed below 400 km/h. Furthermore, the power exponent relating the MPW amplitude to speed has reached 5, significantly exceeding the power exponent of 3 observed below 400 km/h.[5] The nonlinear steepening of the initial wavefront within the tunnel, driven by inertial effects, accounts for the observed changes in the power exponent.[9] Previous research has indicated that MPW emitted from maglev tunnels (operating at 600 km/h) will produce audible sonic booms, posing threats to humans, animals, and building structures near the tunnel exit.[10]

The crucial aspect of mitigating the sonic boom emanating from tunnels is to diminish the wavefront gradient amplitude at the tunnel's exit. Current mitigation strategies encompass installing a hood at the tunnel entrance to lower the initial wavefront gradient,[11,12] alleviating the nonlinear steepening of the wavefront within the tunnel,[13,14] and deploying mufflers at the tunnel's exit.[15,16] Various types of hoods at the tunnel entrance, including flared hoods,[17] oblique hoods,[18] hoods with expanded cross sections,[6] and windowed hoods,[19] have undergone extensive research to mitigate the initial wavefront gradient. Saito *et al.*[6] proposed an improved two-step hood, which involves removing the vertical connection between the first and second hoods and extending the first hood, to better reduce the MPW radiation. Miyachi and Fukuda[19] conducted a multi-objective optimization study on the wavefront gradient within tunnels, focusing on "pattern optimization" of window placement and "area optimization" of spatial distribution to enhance efficiency. The area and location of the window opening are determined according to various ratios between the hood area and the tunnel area. Recently, researchers have integrated bionics inspired by the gills of marine organisms into the exterior design of tunnel portals.[20,21] Kim *et al.*[21] devised a novel hood equipped with air slots on both sides and conducted moving-model experiments. Their findings revealed that the air slots effectively decreased the wavefront gradient amplitude near the inlet. Specifically, the amplitude of the wavefront gradient and MPW were reduced by 56.3% and 78.7%, respectively, upon installing this innovative hood design. Lin *et al.*[22] investigated the mitigating effects of the opening ratio and chamfer angle of the bionic shark-gill hood on MPW. The research indicated that the optimal mitigation effect on MPW was achieved when the hood had an opening ratio of 24% and a hole inclination angle of 16°. More recently, to address the MPW issue in 400 km/h tunnels, Li *et al.*[11] devised a combined hood design that incorporates an enlarged cross section, ventilation windows, and an oblique hat. The study indicates that the best MPW mitigation was achieved with an aperture rate of roughly 15% and a ventilation window distance from the hat being 0.3–0.4 times the length of the enlarged cross section.

The mitigation strategies of sonic booms within the tunnel encompass ballast effects,[13,23] Helmholtz resonator arrays,[14,24–26] and active suction control of the tunnel walls.[1] Fukuda *et al.*[23] conducted an experimental study on the Shinkansen to investigate the influence of ballast on the wavefront steepening rate. The experimental data were used to refine the unsteady friction coefficient in the empirical equation for numerical prediction. Vardy and Brown[13] analogized the ballast effect to a series of Helmholtz resonators. They developed a simplified model for the wavefront evolution in ballasted tunnels, drawing upon the porosity and resistivity properties of the ballast. Subsequently, Tebbutt *et al.*[14] formulated a quasi-one-dimensional model that incorporates nonlinear effects, wall friction, and sound diffusion, while incorporating Helmholtz resonator arrays installed within tunnels. Their findings revealed that a 100 m-long array significantly reduced the wavefront gradient amplitude by 50%. Regarding active flow control, Chen *et al.*[1] introduced suction slots on the tunnel walls to generate a low-pressure zone. This approach successfully reduced the MPW amplitude by 12.4% at 20 m from the tunnel exit.

In recent years, perforated zones at tunnel exits have been utilized to mitigate the MPW intensity.[16,27–29] Ootsuta *et al.*[29] installed an enlarged cross-sectional device at the tube end to attenuate the weak shock wave inside the tube. The device employs porous media material (PMM) coaxial with the tube and forms an air layer with the wall of an enlarged cross section. The wavefront gradient of the weak shock wave is significantly attenuated when passing through the PMM, indicating the device's promising potential for industrial noise suppression. Wang *et al.*[16] utilized two-dimensional simulations to study the effects of perforated exits on tunnel-radiated pressure disturbances. Their findings revealed that the perforated region effectively reduced the MPW magnitude while slightly increasing the pressure amplitude at its top. The study examined three distinct wavefront mitigation configurations, achieving an MPW mitigation rate of approximately 42%. Zhang *et al.*[28] proposed a decreasing open ratio hood to effectively dampen the MPW emanating from the maglev tunnel. This device can reduce the MPW amplitude by 86.7% and 76.2% at 20 and 50 m from the tunnel exit, respectively.

Existing hood designs are aimed at mitigating sonic booms from tunnels operating at speeds under 400 km/h, with scarce research dedicated to reducing sonic booms for 600 km/h maglev tunnels. The windowed hoods at the tunnel portals and the ballast inside the tunnel inspired us to propose a novel porous media hood (PMH). Both possess air permeability and porous structures to achieve the function of mitigating sonic booms, but the parameters of PMH differ in application. For instance, the porosity of the porous media is approximately 0.2 when utilized as a hood,[11,20] whereas it is 0.4 when simulating ballast conditions.[13] Thanks to Ootsuta *et al.*,[29] PMM has already been utilized in designing a muffler structure. However, research on the impact of PMM's intrinsic properties and geometric parameters on MPW remains inadequate. Currently, PMM has been widely applied in various fields such as turbulence stability analysis within channels,[30,31] noise reduction in wind turbine rotors,[32,33] and drag reduction in flow around cylinders.[34] The utilization of PMH to mitigate sonic booms emanating from maglev tunnels remains a novel and worthwhile area of exploration.

In this study, we focus on the effects of the intrinsic properties and geometric parameters of PMH on the mitigation efficiency of MPW, the evolution of flow fields, and the aerodynamic loads on the train body. The rest of this article is structured as follows: Sec. II details the geometric configuration and flow conditions, numerical models and solution parameters, grid resolution, and the validation of numerical results. Section III discusses the influence of porosity, length, and thickness of PMH on the MPW mitigation mechanisms. Furthermore, a comprehensive analysis is conducted on the impact of PMH on the aerodynamic forces and surface pressures of the train, along with an evaluation of the MPW mitigation effectiveness. Finally, conclusions are provided in Sec. IV.

II. METHODOLOGY

A. Geometric configuration and flow conditions

A 1:20 scaled maglev train is considered for investigation, which is consistent with the train model adopted by moving-model

experiments[35] and previous numerical studies.[27] The maglev train maintains its main external configuration, including connecting windshields and magnetic blocks. As illustrated in Fig. 1, taking the train height $H = 0.21$ m as the reference length, the train length L_{tr} and width W are 19.8H and 0.88 H, respectively. The lengths of the head car, middle car, and tail car are 6.95H, 5.9H, and 6.95H, respectively, of which the streamline length is 4H. The other detailed parameters of the computational model are listed in Table I and Fig. 2. The length and area of the double-track tunnel are 75.86H and 0.35 m^2, respectively. The line spacing L_3 is 1.33H. The corresponding blockage ratio, defined as the ratio of the cross-section area of the train to the tunnel, is 0.085.

The maglev train is guided by simplified tracks and travels through the tunnel at a speed of 600 km/h, as illustrated in Fig. 2(a). A pair of porous media hoods (PMH) are installed at both ends of the tunnel, with their internal shape identical to the tunnel. Consequently, the computational domain is divided into a background region, an overset region, and porous media regions. Taking the center point of the tunnel entrance ground as the origin, the x, y, and z axes are defined as the streamwise, spanwise, and vertical directions, respectively. The maglev train is mounted in a $21H \times 1H \times 1.2H$ overset region, with a streamwise distance L_1 of 11.9H between the head train nose and the PMH inlet. The left $71.43H \times 28.57H \times 14.29H$ air domain can ensure flow stability during the initial operation of the train. The corresponding inlet, top, and side planes are all designated as pressure inlet boundaries. To better capture the radiation of the MPW, the outlet air domain adopts a quarter of a sphere with a radius of 47.62H. The pressure far-field is implemented on the outlet to avoid reflection of the MPW. Moreover, the flanges connected to the tunnel are designated as no-slip walls to simulate the mountainous environment.

The PMH parameters considered here contain its porosity, diameter of particles, length L_{PMH}, and thickness h. Only the particle diameter is fixed, while the other parameters will be investigated in Sec. III. Additionally, the evaluation of the aerodynamic effects of the train and tunnel includes the MPW, alternating pressures on the trains and tunnel surfaces, as well as the aerodynamic forces acting on the train. As presented in Figs. 2(b) and 2(c), the positions for acquiring pressure information on the surfaces of the train and tunnel, as well as for the MPW, are all located at a height of $z = 0.65H$. The measurement points on the surfaces of the train and tunnel are uniformly arranged along the streamwise direction. While the MPW measurement points are installed at positions ranging from 0.5 to 2.5 m away from the tunnel exit.

B. Numerical approach and solution settings

1. Governing equations and solution details

The current simulations are executed using the unsteady segregated implicit solver within the finite volume software Star-CCM+. The train speed studied is 0.5 Mach (exceeding 0.3 Mach) and combined with the restraint effect of the tunnel wall, the airflow is designated as compressible flow.[36] The corresponding Reynolds number $Re = \rho V_t H/\mu$, based on the air density ρ (1.177 kg/m^3), the train speed V_t (166.67 m/s), the train height H (0.21 m), and the molecular viscosity μ (1.855×10^{-5} kg/m/s), is 2.2×10^6, which is 1/20 of the full-scale Reynolds number. The current Reynolds number has exceeded 2.5×10^5, as proposed by the CEN standard,[37] and is considered to accurately reflect the aerodynamic effects of a full-scale tunnel.[10]

The improved delayed detached eddy simulation (IDDES) turbulence model based on shear stress transport (SST) k–ω is employed for the current simulation. The IDDES model is a hybrid turbulence model that combines large eddy simulation (LES) and Reynolds-averaged Navier–Stokes equations (RANS), which employs the RANS model within the boundary layer and adopts the LES model in flow separation regions. Previous studies have demonstrated the feasibility of the IDDES model in predicting the flow patterns around the train[20,38] and tunnel aerodynamic effects.[39] The governing equations of the IDDES model are given in the following equation:

$$\frac{\partial(\rho k)}{\partial t} + \frac{\partial(\rho u_i k)}{\partial x_i} = \frac{\partial}{\partial x_i}\left[\left(\mu + \frac{1}{\sigma}\mu_t\right)\frac{\partial k}{\partial x_i}\right] + \tau_{ij}S_{ij} - \frac{\rho k^{3/2}}{l_{RANS}\ \text{or}\ l_{HYBRID}}, \quad (1)$$

where k, u_i, t, μ_t, τ_{ij}, and S_{ij} represent turbulent kinetic energy, velocity, time, turbulent viscosity, stress tensor, and mean strain rate,

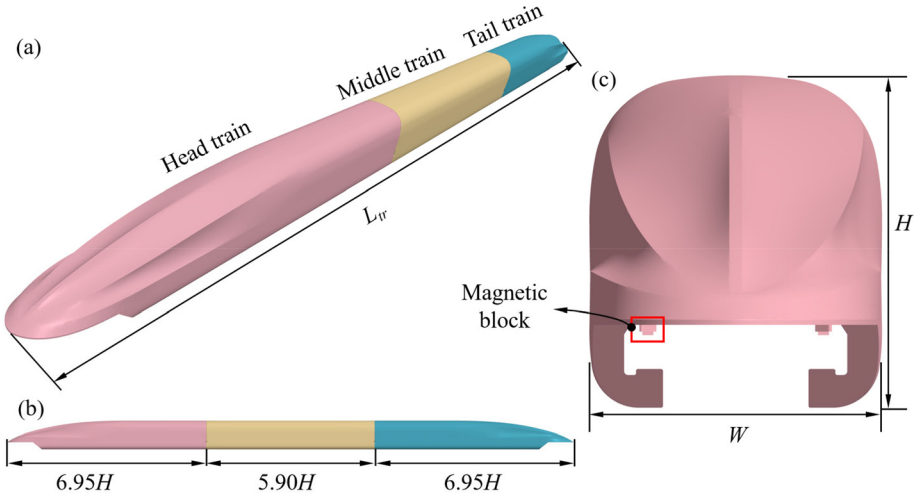

FIG. 1. Geometric model and main reference length parameters of the maglev train: (a) perspective view, (b) side view, and (c) front view.

TABLE I. Dimension of the geometric model and the computational domains. Symbols refer to Figs. 1 and 2.

C	G	K	L_1	L_2	L_3	L_4	L_{tr}	L_{tu}	R_1	R_2	W
71.43H	14.29H	28.57H	11.90H	0.75H	1.33H	0.65H	19.80H	75.86H	1.85H	47.62H	0.88H

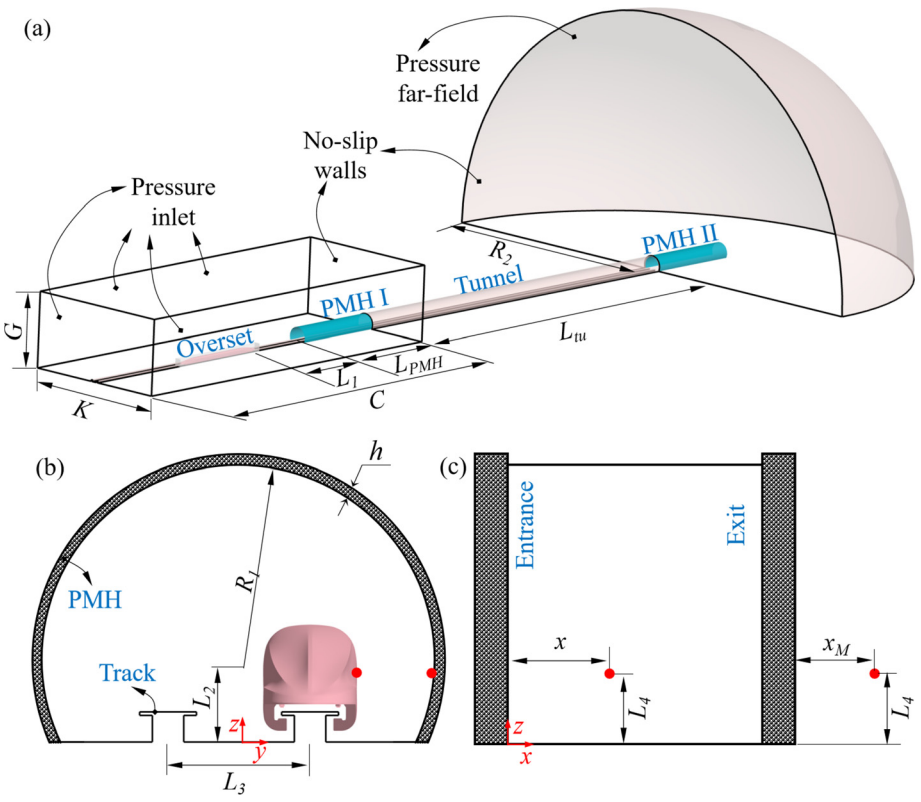

FIG. 2. Computational domain and flow conditions: (a) the coupled computation model of the maglev train and tunnel, as well as its corresponding flow conditions and geometric parameters, (b) schematic diagram of tunnel cross-section and PMH installation, and (c) schematic diagram of the vertical plane of the tunnel with data collection locations for wavefront and MPW.

respectively. The turbulence length scales for the RANS and IDDES models are, respectively, given as $l_{RANS} = \sqrt{k}/\beta^*\omega$ and $l_{HYBRID} = \sqrt{k}/\beta^* f_{\beta^*}\beta^*\tilde{\omega}$, where the model coefficient β^* is 0.09, ω is the unit dissipation rate, and f_{β^*} represents the free-shear modification factor.

The IDDES model employs a delay factor to enhance the distinction between the LES and RANS regions. It achieves wall-modeled LES capabilities by introducing two functions: the blending function f_B and the elevated function f_e. In the near-wall region, the expression of l_{HYBRID} is shown in Eq. (2). Here, the model coefficient C_{DES} is 0.78, and the grid filter Δ_{IDDES} for the sub-grid length-scale is given by Eq. (4). d represents the distance from the wall, while Δ and Δ_{min} are the maximum and minimum distances between the center of the considered grid cell and the centers of its adjacent cells. In the far-wall region, the expression of l_{HYBRID} is shown in Eq. (3). The value of $\tilde{f}_d$ is calculated by Eq. (5), where the model coefficient C_{dt} is 20. For more information about the IDDES model, readers can refer to the theory described by Shur *et al.*,[40]

$$l_{HYBRID} = f_B(1+f_e)l_{RANS} + (1-f_B)C_{DES}\Delta_{IDDES}, \tag{2}$$

$$l_{HYBRID} = \tilde{f}_d l_{RANS} + \left(1-\tilde{f}_d\right)C_{DES}\Delta_{IDDES}, \tag{3}$$

$$\Delta_{IDDES} = \min(\max(0.15d, 0.15\Delta, \Delta_{\min}), \Delta), \tag{4}$$

$$\tilde{f}_d = \max\left(\tanh\left[\left(\frac{C_{dt}\mu_t/\rho}{\sqrt{\nabla u_i : \nabla u_i{}^T}\kappa^2 d^2}\right)^3\right], f_B\right), \tag{5}$$

$$f_B = \min[2\exp(-9\alpha^2), 1], \alpha = 0.25 - d/\Delta. \tag{6}$$

The study adopted a second-order accurate and lower–upper symmetric Gauss–Seidel (LU-SGS) iteration scheme for advancing time. The spatial discretization of the convection term utilizes a hybrid method that blends third-order MUSCL with second-order central differencing for precision. The semi-implicit method for pressure-linked equations (SIMPLE) algorithm is leveraged to tackle the coupling between velocity and pressure in the governing equations. The time step Δt is set to $\Delta t = 1.5 \times 10^{-5}$ s, thereby ensuring that 99% of the grid cells adhere to the Courant–Friedrichs–Lewy (CFL) number is less than 1. Each time step incorporates 25 internal iterations for enhanced accuracy. Before the train nose reached the PMH, the duration L_1/V_t was calculated to ensure that the physical information

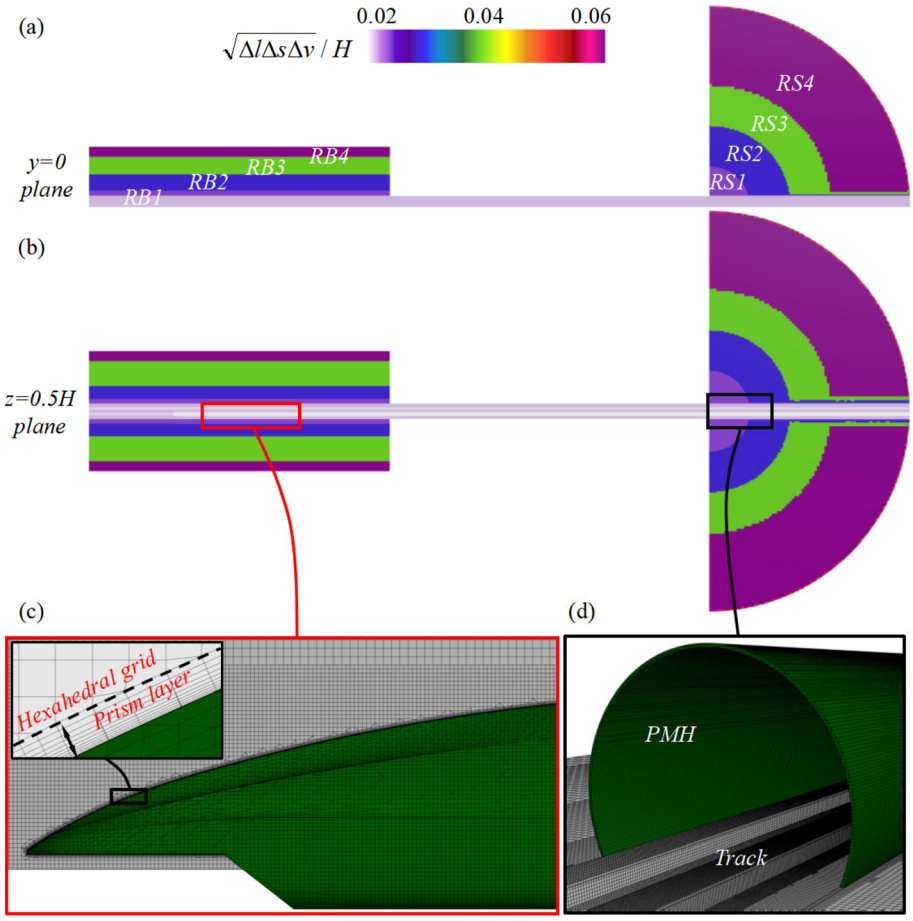

FIG. 3. Spatial encryption distributions and local models' resolution of the medium grid: (a) spatial grid encryption strategy for the $y = 0$ plane, (b) spatial grid encryption strategy for the $z = 0.5H$ plane, (c) grid resolution on the train surface and distribution of prismatic layers, and (d) grid resolution of the PMH and the track. The symbols Δl, Δs, and Δv are defined as the grid size of the streamwise, spanwise, and vertical directions.

within the flow field had fully developed. Thus, the total time taken by the maglev train to traverse the tunnel is $T = (L_1 + L_{tr} + L_{tu} + 2L_{PMH})/V_t$.

2. Numerical model for porous media

Porous media is a continuum containing fluids and fine solid structures. The solid geometric structure is too fine to be individually meshed and fully solved through a computational grid.[33] Therefore, an equivalent numerical model of PMH is utilized for calculation, where additional source terms are introduced into the momentum transport equation to approximately simulate pressure loss.[34,41]

TABLE II. Dimensions of the spatial and boundary layer for computational models.

Grids	Objects	n^+_{mean}	n^+_{max}	Δs^+_{mean}	Δs^+_{max}	Δl^+_{mean}	Δl^+_{max}	Grid number
Coarse	Train	<1.0	1.4	<650	700	<650	700	3.2×10^7
	Tunnel	<1.0	1.8	<750	800	<750	800	
	PMH	<1.0	1.8	<750	800	<750	800	
Medium	Train	<1.0	1.4	<550	600	<550	600	5.4×10^7
	Tunnel	<1.0	1.8	<600	650	<600	650	
	PMH	<1.0	1.8	<600	650	<600	650	
Fine	Train	<1.0	1.4	<400	450	<400	450	7.3×10^7
	Tunnel	<1.0	1.8	<450	500	<450	500	
	PMH	<1.0	1.8	<450	500	<450	500	

One of the classical equations describing fluid flow through porous media is Darcy's law, which relates the flow velocity to the pressure gradient based on a measure of permeability.[42] Darcy law is expressed as Eq. (7) when it is applied to creeping flow ($R_e \ll 1$),

$$-\nabla p = \frac{\mu}{k_p} v_s, \tag{7}$$

where ∇p represents the pressure gradient, k_p represents the permeability of porous media, and vs represents the apparent velocity through the porous media.

The relationship between velocity and pressure gradient becomes nonlinear as the flow velocity increases. Dupuit and Forchheimer proposed adding a quadratic term, as shown in Eq. (8).[42] Equation (8) is commonly named the Forchheimer equation. The factor b must be derived for a specific fluid and related media and is usually determined through experimentation,

$$-\nabla p = \frac{\mu}{k_p} v_s + b\rho |v_s| v_s. \tag{8}$$

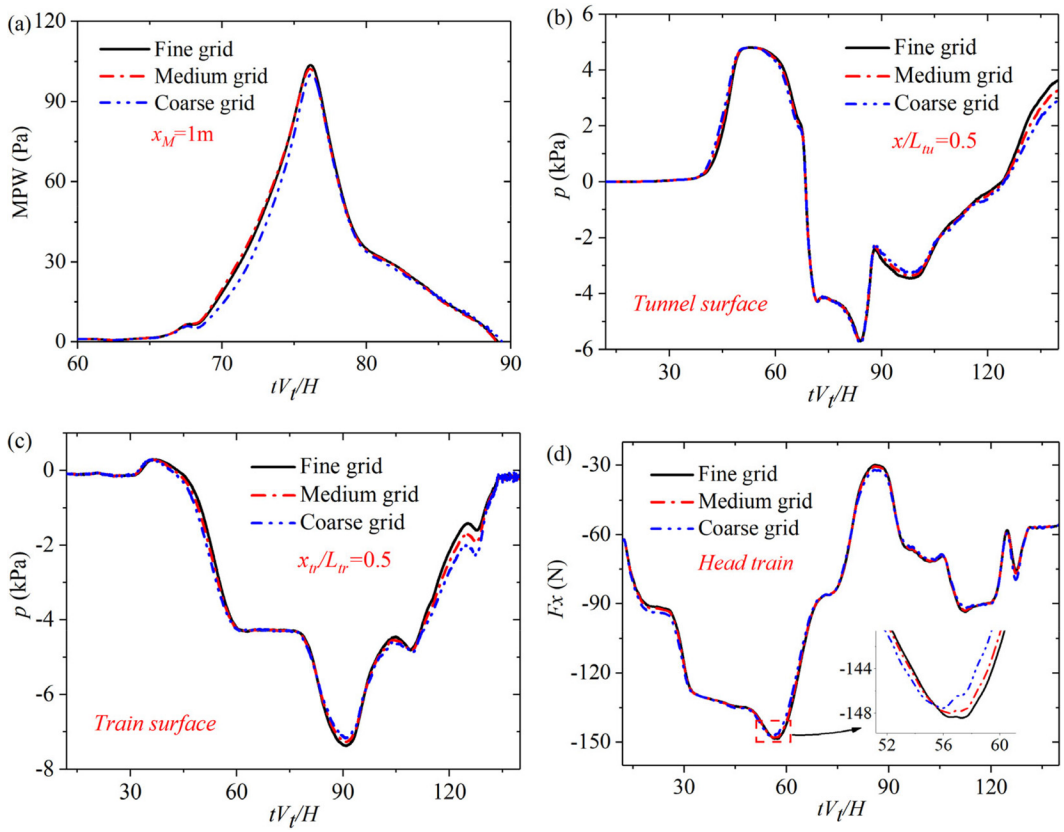

FIG. 4. Grid-independent study of the tunnel aerodynamics effect for the case $L_{PMH} = 3.75$ m: (a) temporal MPW at $x_M = 1$ m location, (b) temporal pressure of the tunnel surface at $x/L_{tu} = 0.5$ position, (c) temporal pressure of the train surface at $x_{tr}/L_{tr} = 0.5$ position, and (d) temporal drag force of the head train. The x_{tr} is defined as the streamwise distance from the train nose to the sampling location.

In the current study, the Ergun equation, which is an example of the Forchheimer equation, is adopted.[42] This is an empirical model for the pressure drop d_p of fluid flowing through a packed bed in the direction of its length L, as presented by the following equation:

$$-\frac{d_p}{L} = P_v + P_i = \frac{150\mu(1-\chi)^2 v_s}{\chi^3 D_p^2} + \frac{1.75\rho(1-\chi)v_s^2}{\chi^3 D_p}, \quad (9)$$

where P_v and P_i are the viscous and the inertial terms, respectively; ρ is the air density; D_p is the average diameter of particles in the porous media; and χ is the volumetric porosity.

By comparing Eqs. (8) and (9), the permeability and b factor in the current study are as Eqs. (10) and (11). Additionally, the porous media is assumed to be homogeneous and isotropic, meaning that the viscous resistance and inertial resistance are the same in all directions,

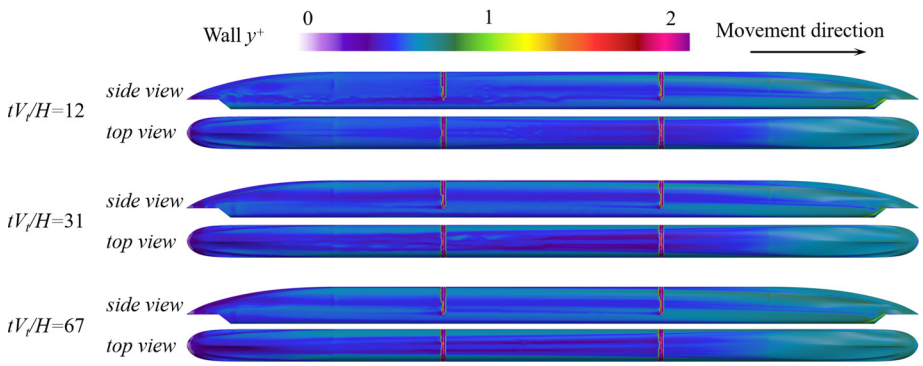

FIG. 5. The distribution of wall y^+ for the maglev train at different operating moments.

$$TKE_{resolved} = 1/2(u'_x u'_x + u'_y u'_y + u'_z u'_z) \quad (12)$$

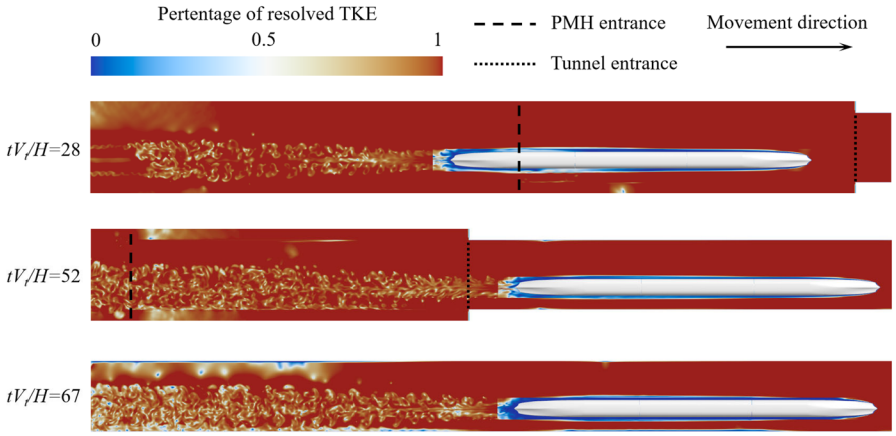

FIG. 6. Percentage of resolved turbulence kinetic energy for the $z = 0.6H$ plane.

$$k_p = \frac{\chi^3 D_p^2}{150\mu(1-\chi)^2}, \quad (10)$$

$$b = \frac{1.75\rho(1-\chi)}{\chi^3 D_p}. \quad (11)$$

C. Grid resolution

1. Grid strategy and grid independence

The grid resolution and spatial encryption strategy for the computational domain are shown in Fig. 3. Hexahedral grids are utilized for the discretization of overset regions, porous media regions, and the background region. To achieve a smooth transition of the grid, the computational domain is spatially partitioned into successive encryption zones. A medium grid resolution is displayed here to demonstrate the grid strategy. The isotropic grid sizes for the overset region, tunnel, refinement block 1 (*RB1*), *RB2*, *RB3*, and *RB4* are 0.05*H*, 0.05*H*, 0.05*H*, 0.1*H*, 0.2*H*, and 0.4*H*, respectively. To accommodate the spherical radiation characteristics of MPW, the isotropic grid sizes for refinement sphere 1 (*RS1*), *RS2*, *RS3*, and *RS4* are 0.05*H*, 0.1*H*, 0.2*H*, and 0.4*H*, respectively. The isotropic grid size near the running track is set to 0.025*H*, to accurately capture train aerodynamic forces under extremely small track clearances.[20]

Three sets of grids, including coarse, medium, and fine grids, have been employed to assess the validity of the simulation approach, with their detailed specifications outlined in Table II. These three grids share identical construction principles and wall-normal resolutions, differing solely in their spatial grid resolutions. To precisely analyze the near-wall flow structures, a prism layer consisting of 15 protruding elements with a growth rate of 1.2 and a total height of 0.03*H* has been generated near the train, PMH, and tunnel walls. The distance from the center of the first grid layer to the wall, denoted as n, is $3.5 \times 10^{-4}H$, which ensures that the average dimensionless resolution in the wall-normal direction $n^+_{mean} < 1$. Here, n^+ is defined as $n^+ = n\mu_\tau/\nu$, where μ_τ is the friction velocity and ν is the dynamic viscosity. Moreover, the parameters of the streamwise ($\Delta l^+ = \mu_\tau \Delta l/\nu$) and the spanwise ($\Delta s^+ = \mu_\tau \Delta s/\nu$) dimensionless resolution are summarized in Table II. Thus far, the grid strategy, encompassing wall resolution and spatial encryption regions, has been thoroughly elaborated upon.

The effect of PMH on tunnel aerodynamics is employed in a grid independence study at $V_t = 600$ km/h. Drawing from the material parameters of PMH utilized in the experiments by Ootsuta *et al.*,[29] the PMH employed here has a particle diameter of 1.4 mm, a porosity of 0.2, a length of 3.75 m, and a thickness of 3.5 mm. The detailed PMH numerical model is described in Sec. II B. As depicted in Fig. 4, a comparative analysis is presented for the MPW, pressures on the train and tunnel surfaces, and aerodynamic forces acting on the train, across the three sets of grids. Dimensionless time tV_t/H, pressure p, and drag force Fx are employed for description. The medium and fine grids exhibit excellent agreement in predicting the tunnel's aerodynamic effects, while the coarse grid yields predictions with minor deviations from the other two. For the three sets of grid resolutions, the differences in the extreme values of MPW at $x_M = 1$ m, pressure at the

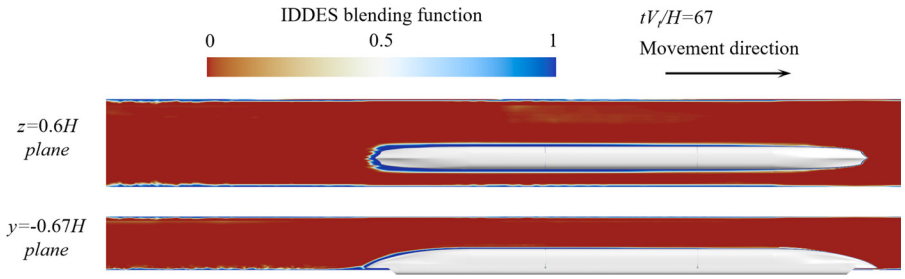

FIG. 7. The distribution of the IDDES blending function around the train.

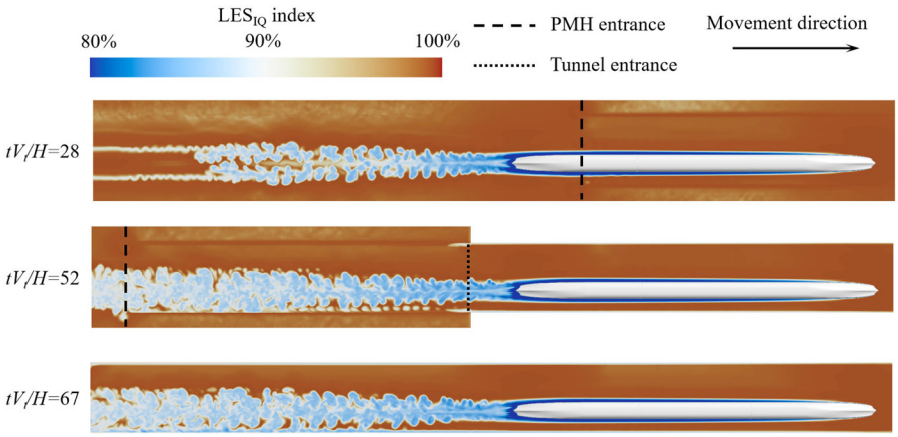

FIG. 8. The distribution of the LES$_{IQ}$ index for the $z = 0.6H$ plane.

middle of the tunnel, pressure at the middle of the train, and drag force on the head train are 2.3%, 1.2%, 2.8%, and 1.6%, respectively. Based on a comprehensive comparison of the above data, the medium grid strategy is adopted for subsequent discussions to achieve the optimal balance between computational cost and prediction accuracy.

As the maglev train moves through the tunnel, the continuous variation in their relative positions makes it impractical to use an average wall y^+ value to assess the resolved state of wall turbulence. To illustrate the instantaneous distribution of y^+ when the train is positioned in open space, the PMH zone, and within the tunnel, three moments are chosen. As depicted in Fig. 5, the overall y^+ value across the train's surface remains below 1 at three instantaneous times. A higher y^+ value is observed solely at the windshield position. This demonstrates that the prism layer employed in the grid strategy fulfills the requirements of IDDES for simulating near-wall flow.

2. Resolved turbulent kinetic energy

Pope[43] suggested that the percentage of the resolved turbulent kinetic energy (TKE) to the total TKE exceeding 80% represents a good accuracy of LES for eddy-resolving simulation. The percentages of the resolved TKE around the maglev train and wake region are shown in Fig. 6. Three typical moments are represented, where the train wake is in open space, within the PMH region, and inside the tunnel, respectively. The resolved TKE is defined by Eq. (12), where u'_x, u'_y and u'_z represent the velocity fluctuations in the three directions. Most of the percentages of the resolved TKE around the train are greater than 80%, which confirms that the grid resolution is suitable for IDDES simulation.

The interface between RANS and LES, as well as how to smoothly and accurately transfer turbulence stress information, is a core issue. IDDES achieves wall-modeled LES capability by introducing the blending function f_B and the elevated function f_e. The blending function f_B, as defined in Eq. (6), can be used to evaluate the transition and continuity

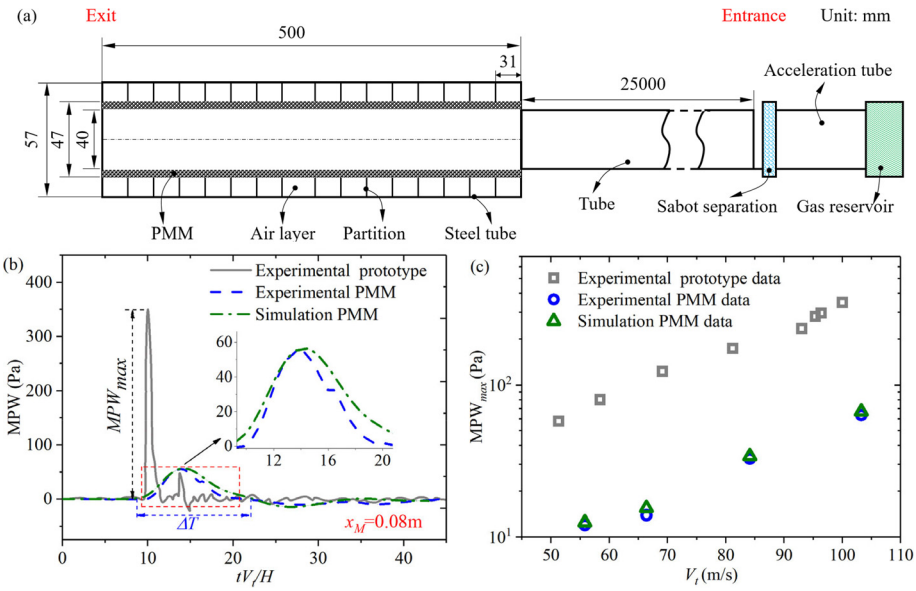

FIG. 9. Numerical validation of PMM's mitigating effect on MPW: (a) experimental schematic of installing a PMM at the end of the train/tunnel simulator, (b) the evolution of MPW under the simulated and experimental PMM effect at $V_t = 100$ m/s, and (c) validation of the mitigation effect of PMM on MPW under different train speeds.

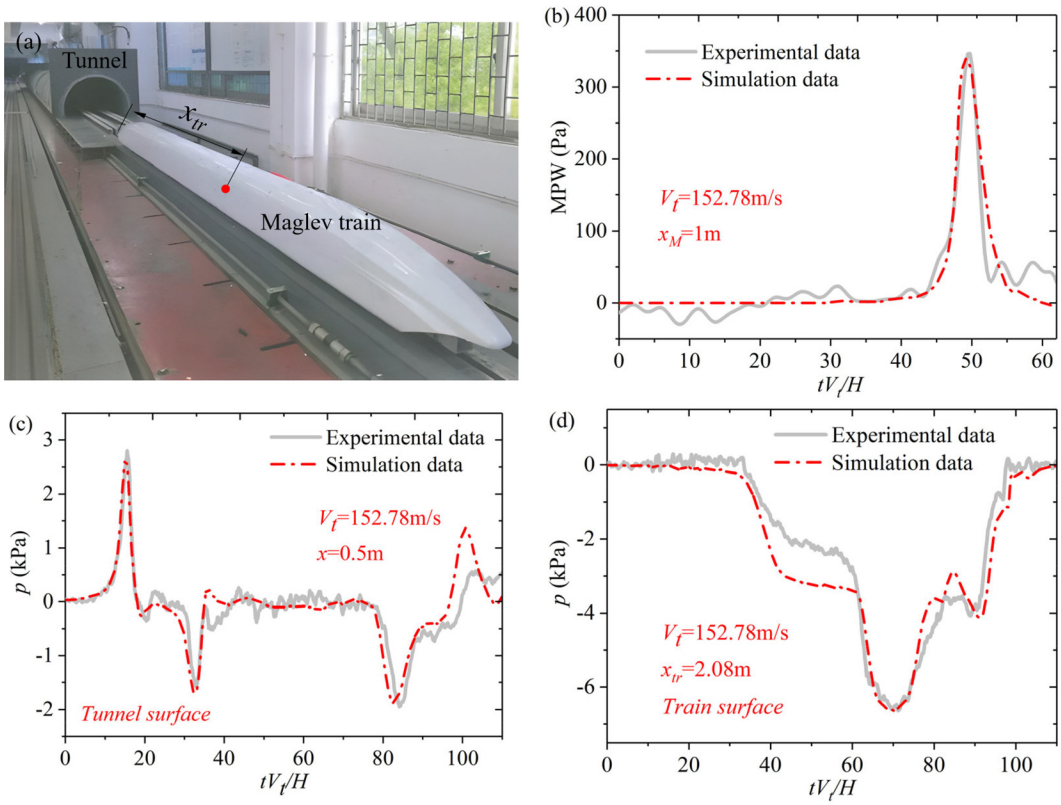

FIG. 10. Comparison of the data between the simulation and moving-model experiments at $V_t = 152.78$ m/s: (a) experimental train and tunnel models, (b) evolution of MPW at $x_M = 1$ m location, (c) temporal pressure of the tunnel surface, and (d) temporal pressure of the train surface.

between RANS and LES regions. Figure 7 shows the distribution of the blending function around the train at $tV_t/H = 67$. A blending function value approaching 0 denotes the LES region, whereas a value near 1 signifies the RANS region. Intermediate values indicate a smooth and continuous transition between the RANS and LES regions. The grid resolution in the near-wall region is insufficient for utilizing the LES model for solving. As indicated by the blue region in Fig. 7, the RANS model is utilized to provide accurate boundary flow resolution. Furthermore, the distributions of the RANS region near the train surface and the tunnel wall in Fig. 7 align with the lower resolved TKE shown in Fig. 6. This consistency is also evident in the blending function and resolved TKE distributions of the LES region,

$$TKE_{resolved} = 1/2\left(u'_x u'_x + u'_y u'_y + u'_z u'_z\right), \tag{12}$$

3. LES_{IQ} index

Celik *et al.*[44] proposed the LES_{IQ} index to evaluate the quality of LES and suggested that 75%–85% of LES_{IQ} was suitable for most high Reynolds number engineering applications. The LES_{IQ} index is defined as follows:

$$LES_{IQ} = \left[1 + a_v\left(\frac{v_{sgs} + v}{v}\right)\right]^{-a_e}, \tag{13}$$

where empirical constants a_v and a_e are 0.05 and 0.53, respectively; and v_{sgs} is the sub-grid viscosity. A LES_{IQ} value below 80% indicates very large-eddy simulation (VLES), while a value above 80% signifies an appropriate LES with near-wall resolution (LES-NWR), and a value exceeding 95% implies direct numerical simulation (DNS).[45]

Figure 8 shows the distribution of the LES_{IQ} index for the plane at $z = 0.6H$. The flow separation region solved using the LES model is basically greater than 80%, achieving good LES quality. The RANS model is used to solve the flow near the train wall, so the result of LES_{IQ} being less than 80% is expected and does not affect the aerodynamic results of the train. Overall, the y^+ distribution on the train surface, the resolved TKE distribution, and the LES_{IQ} index validate the credibility of the eddy-resolving approach.

D. Validation of numerical results

1. Validation of porous media model

Despite the previously discussed grid independence test, further validation is required to ensure the accuracy of the porous media model and its calculations of the tunnel aerodynamic effects. The initial focus is on validating the porous media model and evaluating its effectiveness in mitigating MPW issues. The verification of the influence of PMM on MPW was compared with the experimental data of a 1:300 scaled train/tunnel simulator at the Institute of Fluid Science,

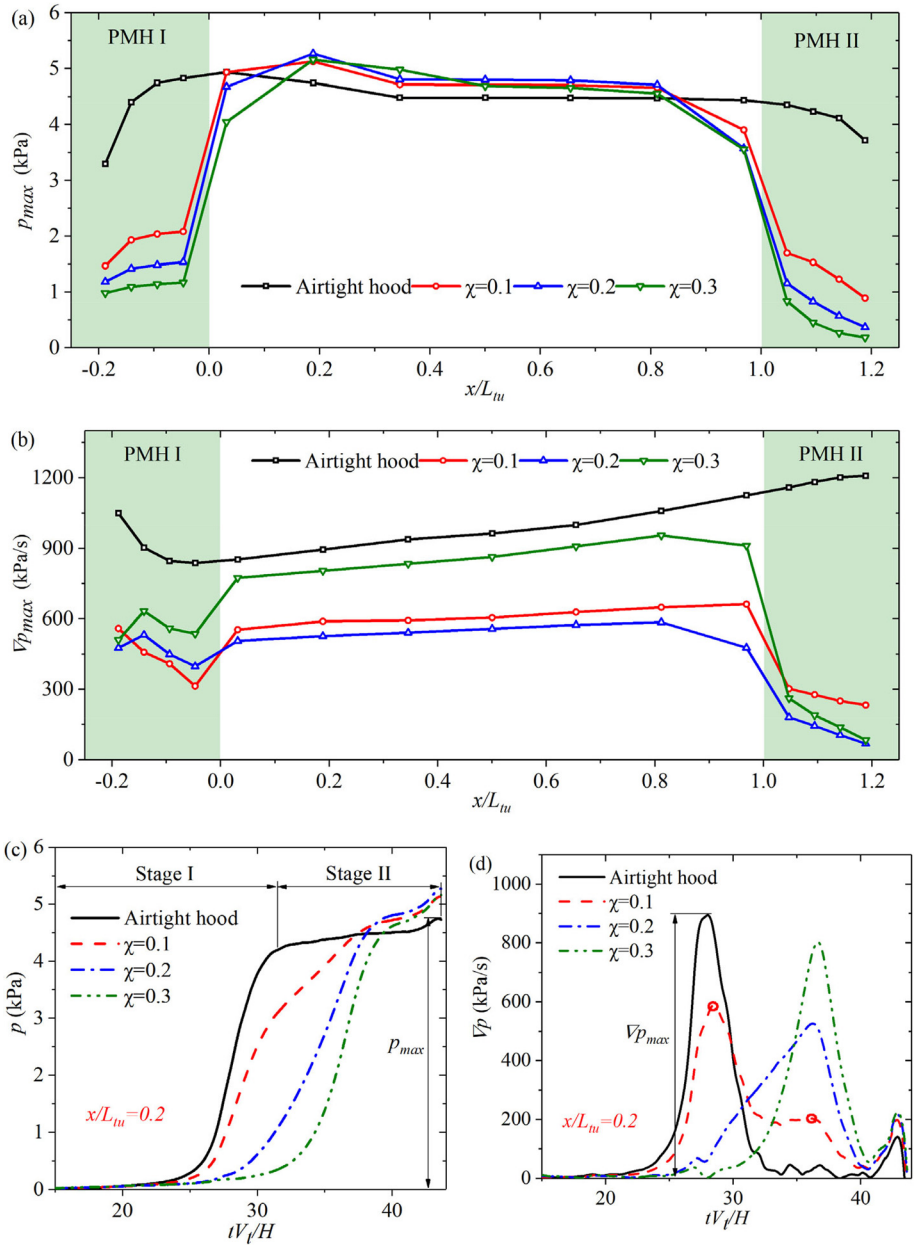

FIG. 11. Influence of porosity on the wavefront characteristics: (a) distribution of the wavefront amplitude, (b) distribution of the wavefront gradient amplitude, (c) the wavefront evolution at $x/L_{tu} = 0.2$ location, and (d) the wavefront gradient evolution at $x/L_{tu} = 0.2$ location.

Tohoku University.[29,46] As illustrated in Fig. 9(a), the train is propelled by pressurized nitrogen from the gas reservoir, accelerates through a designated section, and then enters the tube after sabot separation. The train comprises a cylindrical piston measuring 18 mm in diameter and 200 mm in length. The tube, with a diameter of 40 mm, yields a blockage ratio of 0.2. Installed at the tube's end is a 500 mm-long dual-coaxial tube. The inner tube, featuring a porous plastic, boasts an inner diameter of 40 mm and a wall thickness of 3.5 mm. The surrounding outer tube, crafted from low-carbon steel, measures 57 mm in diameter. The air layer between the dual-coaxial tubes is partitioned by baffles spaced 31 mm apart. These baffles not only augment the attenuation of MPW but also act as stabilizers for the PMM. The porosity and average particle diameter of the porous plastic are 0.2 and 1.4 mm, respectively. For detailed parameters related to the experiment and the porous plastic, please refer to Ootsuta *et al.*[29]

Figure 9(b) shows the comparison of the experimental and simulated temporal MPW under the effect of PMM at $V_t = 100$ m/s. ΔT is defined as the duration of the MPW. Compared to the prototype tube data, PMM reduces the extreme values of MPW and increases the duration time ΔT. The PMM located at the tube outlet effectively mitigates the wavefront gradient. Meanwhile, potential Helmholtz resonators[14,24] are formed between the air layer and the PMM in conjunction

with the baffle. Compared to the data without any intervention, the application of PMM results in an 80% reduction in the MPW amplitude at $x_M = 0.08$ m location and a sixfold increase in ΔT. Additionally, the MPW amplitude data under the influence of PMM at four different train speeds are summarized in Fig. 9(c). The corresponding errors between the experimental and simulated MPW amplitudes are within 3.9%. Therefore, the IDDES model's predictive accuracy for MPW and the numerical model of porous media have both demonstrated their reliability and validity.

2. Moving-model experiments

To validate the simulation of aerodynamic effects resulting from the coupling of maglev trains and tunnels, we conducted moving-model experiments at the Key Laboratory of Rail Transit Safety, affiliated with the Ministry of Education at Central South University. The 1:20 scale model of the maglev train and tunnel [see Fig. 10(a)] remains consistent with the model parameters described in Sec. II A. The experimental equipment, comprising the launching section, braking section, and exhaust section, has obtained CNAS international certification (Certificate Number: CNAS L 10220).[35] The lengths of the acceleration section, test section, and braking section are 33, 54, and 24 m, respectively. The Reynolds number is 2×10^6 based on a train speed of $V_t = 550$ km/h, which also exceeds the CEN standard[37] of 2.5×10^5. The Honeywell DC030NDC4 differential pressure sensors were utilized to acquire pressure information, with a precision of 0.5%. The pressure sensors feature a measurement range of ±7500 Pa, with the sampling frequency configured at 10 000 Hz. For detailed data regarding the maglev moving-model experimental equipment, readers may refer to the descriptions in previous literature.[35]

Figure 10 presents a comparative analysis of simulation and experimental data about MPW, tunnel wall pressure, and train surface pressure at $V_t = 550$ km/h. The MPW measurement is installed at the $x_M = 1$ m location, the tunnel wall measurement at the $x = 0.5$ m position, and the train measurement at its streamwise central position. The simulation and experimental data exhibit remarkable consistency in both their developmental trends and amplitudes among the comparisons. Regarding the extreme value errors of the simulation and experimental data, the MPW, tunnel wall pressure, and train surface pressure exhibit errors of 1.1%, 2.5%, and 1.3%, respectively. Based on comprehensive grid-independent tests and experimental data validation, the prediction capabilities of both the porous media model and IDDES model have been verified for their correctness and reliability.

III. RESULTS AND DISCUSSION

The parameters of PMH mainly include its properties (porosity and particle diameter) and configuration parameters (length and

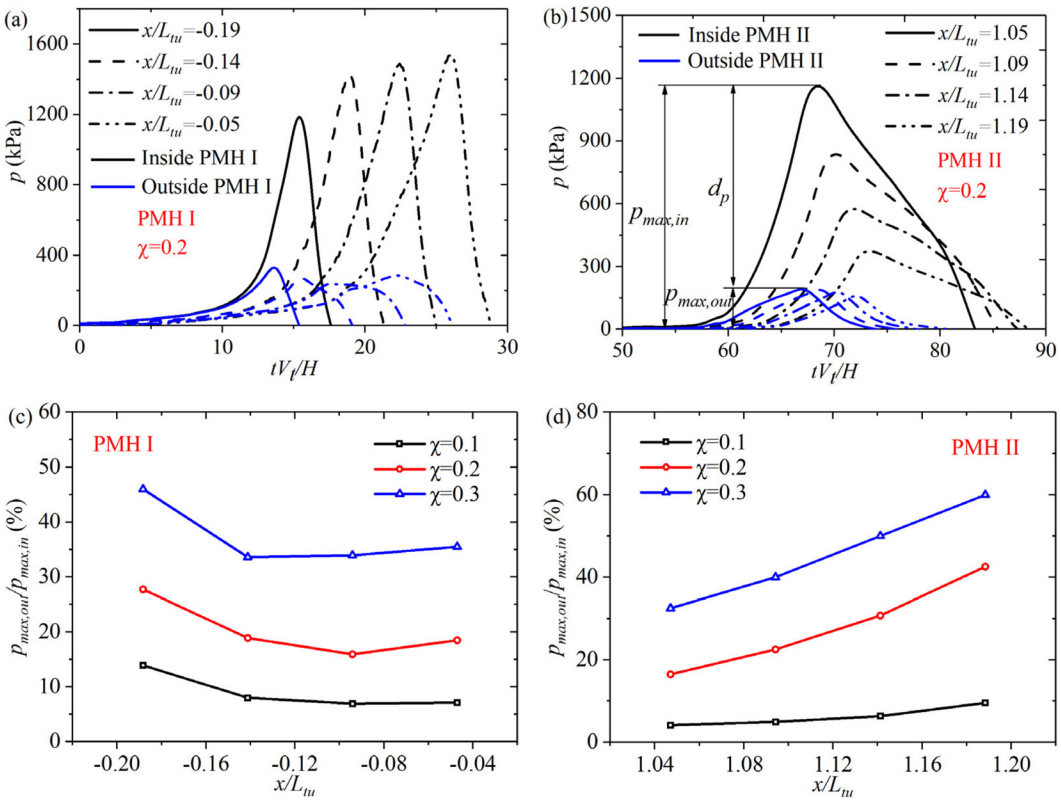

FIG. 12. Pressure comparisons on both sides of the PMH as the initial wavefront passes through it: (a) temporal pressure along the streamwise direction on both sides of the PMH I at $\chi = 0.2$ condition, (b) temporal pressure along the streamwise direction on both sides of the PMH II at $\chi = 0.2$ condition, (c) the release rate of the initial wavefront along the streamwise direction of the PMH I, and (d) the release rate of the initial wavefront along the streamwise direction of the PMH II.

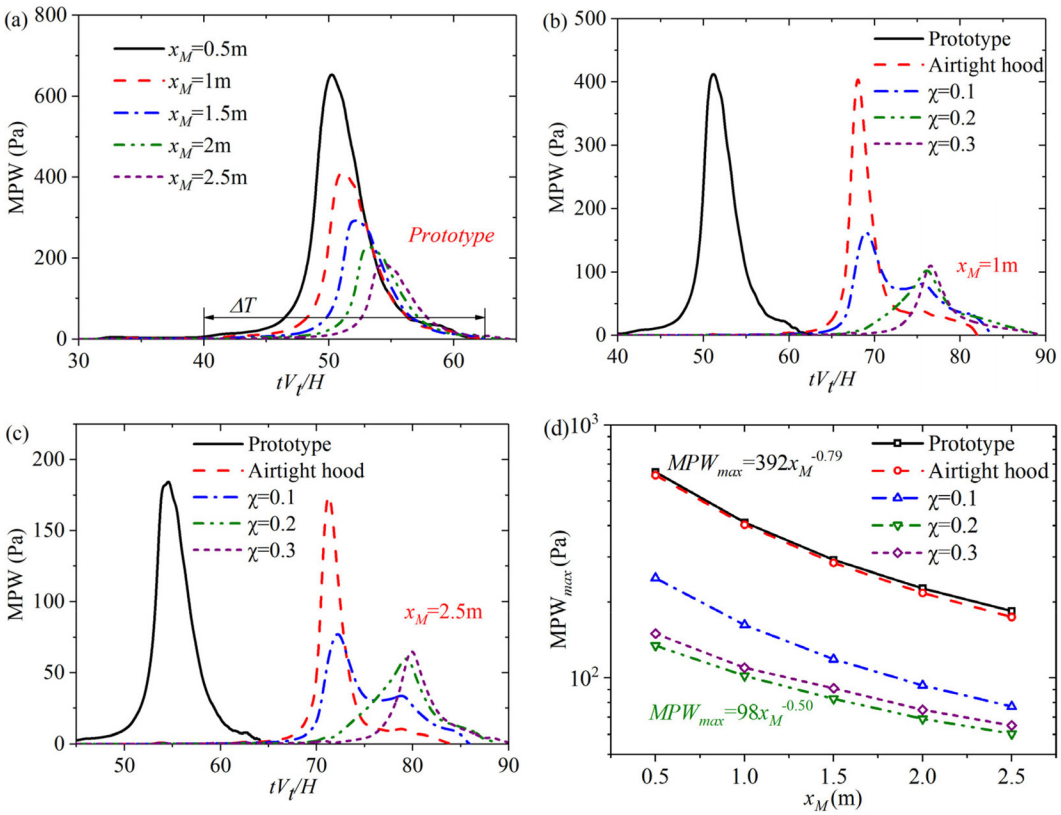

FIG. 13. Influence of porosity on the MPW characteristics at $V_t = 600$ km/h: (a) temporal prototype MPW at different sampling locations, (b) temporal MPW under different porosity at $x_M = 1$ m location, (c) temporal MPW under different porosity at $x_M = 2.5$ m location, and (d) the distribution of MPW amplitude along the streamwise direction under different porosities.

thickness). The particle diameter of PMH is 1.4 mm here. The effects of other PMH parameters on MPW are fully discussed in this section.

A. Influence of PMH porosity

1. Wavefront characteristics

The effects of PMH porosity on the wavefront behavior, MPW characteristics, and the evolution of flow fields are discussed. The length of PMH is 3.75 m, and the thickness is 3.5 mm. An airtight hood was established as the control group to contrast the impacts of PMH on tunnel aerodynamic performance. The initial wavefront, arising from the train's entry into the tunnel or the PMH, initially travels toward the tunnel exit at the speed of sound. Their propagation velocity will surpass the speed of sound as local pressure disturbances intensify.[9] Consequently, as depicted in Fig. 11(b), these localized pressures result in a gradual steepening of the wavefront along the tunnel.

Figures 11(a) and 11(b) show the wavefront amplitude and the wavefront gradient amplitude along the streamwise direction, respectively. The green zones at the left and right ends of the figures represent the PMH at the entrance and exit, respectively. The PMH, owing to its permeability, exerts a pressure-relieving effect on the initial wavefront. The percentage reduction in the initial wavefront amplitude within the PMH zones also rises as porosity increases.[47] Nonetheless, a $\chi = 0.2$ of PMH I zone yields the smallest wavefront gradient amplitude within the tunnel. This suggests that porosity of 0.2 facilitates an optimal transition from the ventilated area to the sealed environment of the tunnel. This aligns with the findings of researchers who have explored the effects of entrance ventilation windows on MPW,[11,20] concluding that an opening ratio of roughly 0.2 offers the most beneficial outcome. Furthermore, the wavefront gradient mitigation rate within the PMH II region exhibits a positive correlation with increasing porosity. Nevertheless, this study focuses on a double-track tunnel, where uniformity of PMH porosity across both ends is crucial. A significant increase in porosity within the PMH II region may pose the risk of another strong MPW. Consequently, the minimum wavefront gradient amplitude at the tunnel exit [shown in Fig. 11(b)] confirms that porosity of 0.2 achieves the best MPW mitigation rate.

To explain the above phenomenon, Fig. 11(c) shows the effect of different porosity on the temporal wavefront at the $x/L_{tu} = 0.2$ location. The sharp increase in Stage I is attributed to the entry of the streamlined head into the PMH I region, while the subsequent rise in Stage II is due to the main body of the train entering the PMH I region. The porosity mainly reduces the initial wavefront gradient by prolonging the duration of Stage I and shortening the duration of Stage II. For the $\chi = 0.1$ scenario, the insufficient decompression of the initial wavefront within the PMH I region leads to a marginal improvement in

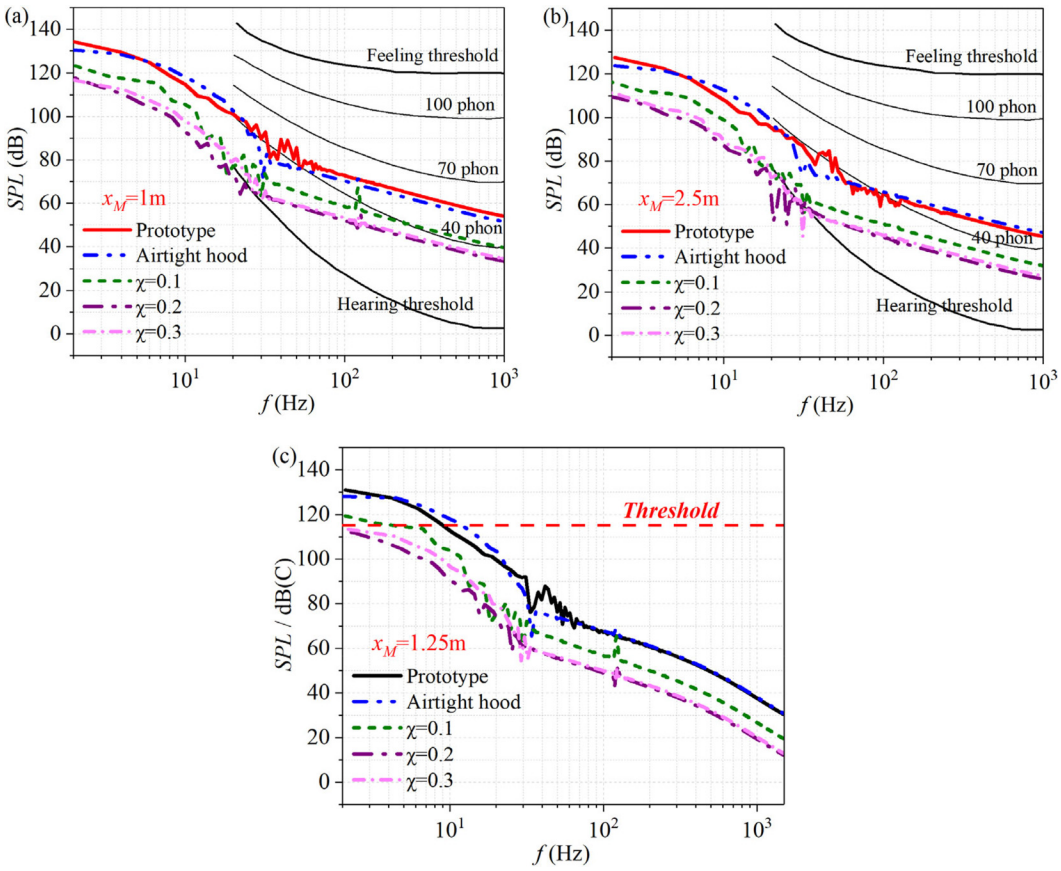

FIG. 14. Influence of porosity on the MPW SPL: (a) unweighted SPL at $x_M = 1$ m position referenced to equal-loudness-level contours, (b) unweighted SPL at $x_M = 2.5$ m position referenced to equal-loudness-level contours, and (c) C-weighted SPL at $x_M = 1.25$ m position referenced to European directive 2003/10/EC.

wavefront gradient reduction. In contrast, the $\chi = 0.2$ scenario effectively facilitates gradual decompression of the initial wavefront, ensuring a seamless transition between the PMH I region and the main tunnel section. For the $\chi = 0.3$ case, it appears that the pressure gradient relief of the PMH has ceased to be effective. The initial wavefront at the location of $x/L_{tu} = 0.2$ more closely resembles the fluctuations generated when the streamlined head of the train enters the main tunnel section. As depicted in Fig. 11(d), the wavefront gradient profiles at $x/L_{tu} = 0.2$ location for PMH cases exhibit a notable reduction in their amplitudes compared to the airtight hood scenario. Specifically, the wavefront gradient amplitudes are diminished by 34.1%, 41.4%, and 10.2% for porosities of 0.1, 0.2, and 0.3, respectively. The timing of the peak wavefront gradient shifts later as the porosity increases. It is crucial to observe that the wavefront gradient of the $\chi = 0.1$ scenario features two distinct local peaks (shown as two red circles). The first local peak arises at a time close to that of the airtight hood case, whereas the second local peak aligns with the timing of the $\chi = 0.1$ and $\chi = 0.2$ scenarios. This aligns well with the findings presented in Fig. 11(c).

Understanding the pressure variations both internally and externally within the PMH zones during the passage of the initial wavefront is equally paramount. Figures 12(a) and 12(b) depict the temporal wavefront on either side of the PMH zones for $\chi = 0.2$ case. $p_{max,in}$ and $p_{max,out}$ are defined as the wavefront amplitude, measured, respectively, within and outside the PMH wall. The corresponding d_p represents the pressure drop experienced by the wavefront in the normal direction across the PMH. The magnitude of $p_{max,in}$ progressively diminishes toward the ends of the PMH, with a more pronounced decline observed in the PMH II region. Conversely, the amplitude of $p_{max,out}$ remains relatively stable, leading to a non-constant ratio between $p_{max,out}$ and $p_{max,in}$. The varying pressure drop across the PMH region can be attributed to the wavefront's transient nature as an excitation source, distinct from a steady-state airflow.[48] Consequently, the pressure drop within the PMH region does not maintain a uniform value across different locations. Figures 12(c) and 12(d) demonstrate that increasing porosity leads to a reduction in pressure drop, thereby enhancing the ratio between $p_{max,out}$ and $p_{max,in}$.

2. MPW characteristics

The temporal MPW in the streamwise direction of the prototype case is depicted in Fig. 13(a). Across the five locations, the duration ΔT of the MPW remains relatively consistent, approximately 2.8×10^{-2} s. The MPW amplitudes exhibit distinct values, with 412 Pa at $x_M = 1$ m and 184 Pa at $x_M = 2.5$ m. In aircraft sonic booms, the N-shaped wave

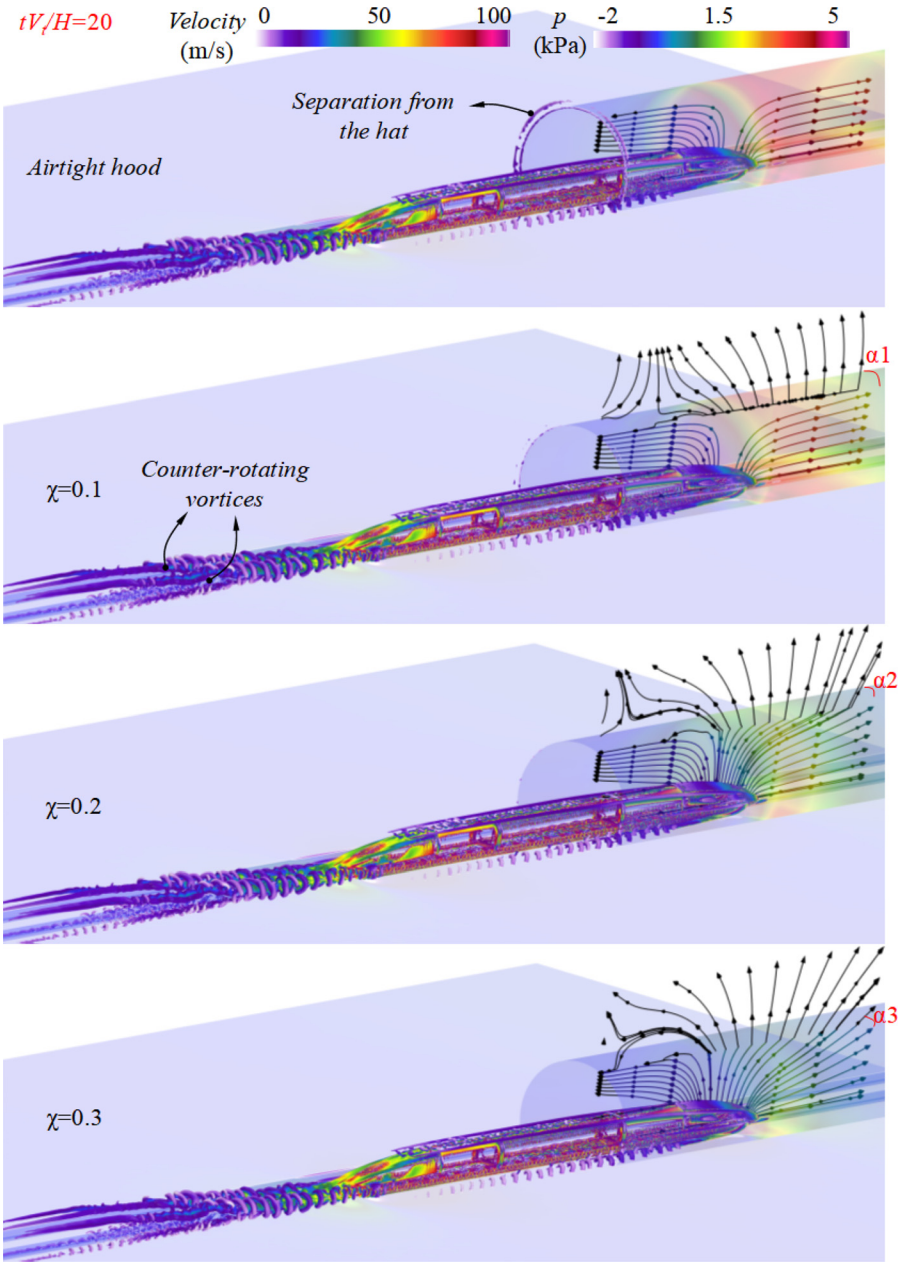

FIG. 15. The influence of different porosity on the initial wavefront and the flow field around the train. Instantaneous iso-surfaces generated by the Q-criterion are colored by the velocity magnitude ($Q = 1.5 \times 10^5$). The train and PMH are rendered based on pressure. The photographs are recorded $tV_t/H = 20$.

commonly exhibits an amplitude on the order of 10^2 Pa and a duration spanning from 10^{-4} to 10^{-2} s.[49] Therefore, the MPW radiated by the prototype tunnel at $V_t = 600$ km/h exceeds the standard threshold at the specified locations,[10] resulting in audible sonic booms. The influence of porosity on the MPW characteristics is shown in Figs. 13(b) and 13(c). Compared to the prototype scenario, an augmentation of the PMH at both extremities results in a peak occurrence delay ($tV_t/H = 18$) in the airtight hood case. The occurrence time of the MPW peak is delayed with increasing porosity. The spatial distribution of MPW amplitude along the streamwise direction under different porosities is shown in Fig. 13(d). The $\chi = 0.2$ case exhibits the best MPW mitigation rate. Compared to the prototype case, the MPW amplitudes at $x_M = 1$ m and $x_M = 2.5$ m in the $\chi = 0.2$ case are reduced by 75.2% and 67.3%, respectively.

Based on our previous research,[10] the sound pressure level (SPL) has been used to discuss the spectral characteristics of MPW. The SPL is derived from the formula $\mathrm{SPL} = 20lg(p/p_r)$, where p_r represents the reference sound pressure, typically set at 2×10^{-5} Pa. Among them, the unweighted SPL is used for comparison with the equal-loudness-level contour of the human ear,[50] while the C-weighted SPL is used for comparison with the European directive 2003/10/EC.[51] The equal-loudness-level contour of the human ear is a curve that represents the

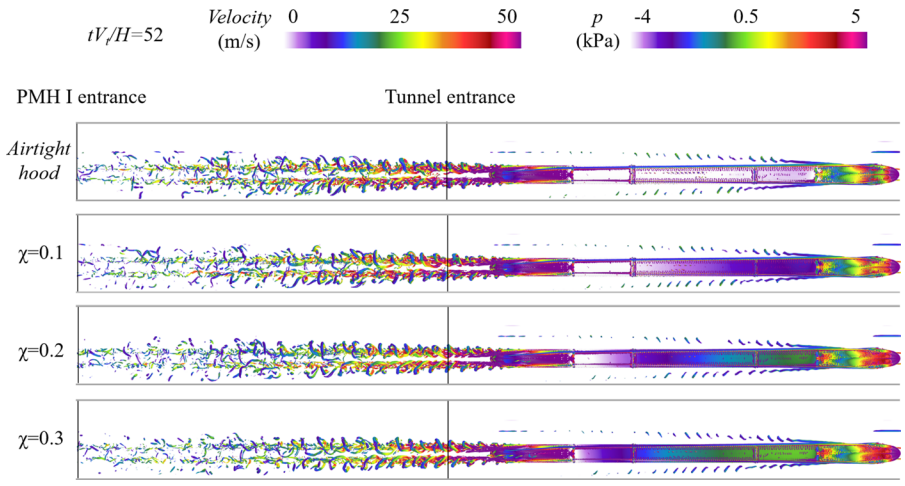

FIG. 16. The influence of porosity on the wake flow and the slipstream. Instantaneous iso-surfaces generated by the Q-criterion are colored by the velocity magnitude ($Q = 6 \times 10^5$). The train is rendered based on pressure. The photographs are recorded $tV_t/H = 52$.

relationship between the SPL and frequencies of pure tones of different frequencies. European directive 2003/10/EC specifies that a lower actuation level should not exceed 135 dB(C) near the tunnel exit. Furthermore, the C-weighted sound peak level should not exceed 115 dB(C) at 25 m from the tunnel exit.

Therefore, Figs. 14(a) and 14(b) illustrate unweighted SPL and Fig. 14(c) presents the C-weighted SPL under the influence of the PMH. The SPL of the prototype tunnel's MPW has already exceeded the hearing threshold at $V_t = 600$ km/h, generating an approximately 55 Phon loudness level of the sonic boom at the $x_M = 1$ m location. The case of $\chi = 0.2$ effectively reduced the SPL at the positions of $x_M = 1$ m and $x_M = 2.5$ m. Although the SPL at both positions still exceeds the hearing threshold, the use of the case with $\chi = 0.2$ has significantly reduced their loudness level. From the perspective of C-weighted SPL, neither the $\chi = 0.2$ case nor the $\chi = 0.3$ case exceeded 115 dB(C) in terms of sound peak level at $x_M = 1.25$ m position. Consequently, employing PMH with a porosity of 0.2 efficiently mitigates the sound pressure level of MPW, aligning it with the standards stipulated in the European directive 2003/10/EC.

3. The evolution of flow field

To explore the influence of porosity on the generation of initial wavefronts, Fig. 15 provides a detailed description from the perspectives of the instantaneous pressure field, flow trend, and vortex structures at $tV_t/H = 20$. Given the breathability of the PMH material, the high pressure from the initial wavefront can dissipate outward within the PMH I region. The initial wavefront in front of the train nose progressively diminishes as porosity increases. In the case of an airtight hood, a fraction of the airflow near the train nose travels forward due to the train's propulsion, while the remaining portion is compressed and directed outward beyond the PMH I exit. Conversely, in the $\chi = 0.1$ scenario, the forward and outward airflows generate an additional branch that flows outward along the normal direction of the PMH I wall. As porosity increases further, the angle between the airflow direction and PMH I gradually narrows ($\alpha 1 > \alpha 2 > \alpha 3$), suggesting that higher porosity enhances the outward diffusion of local airflow. The flow structures around the train can be divided into the flow separation vortices caused by the streamlined head, small-scale vortices near the track attachments, the counter-rotating wake vortices, and the separation vortices near the hat. The PMH I region inhibits the separation of vortices near the hat to a certain extent. The impact of PMH on vortex structures requires selecting a moment when the train has completely entered the PMH I region for analysis, such as in Fig. 15.

Instantaneous iso-surfaces rendered by velocity amplitude are used to demonstrate the influence of porosity on the train wake and slipstream at $tV_t/H = 52$, as shown in Fig. 16. The wake length of the train operating within the tunnel has exceeded the train length,[52] resulting in significant slipstream interference. The PMH I region, with its air permeability, drastically mitigates the amplitude of the slipstream generated by the train's wake. Additionally, the diffusion area of the vortex structures within the wake is constrained, and this effect intensifies with an increase in porosity. Furthermore, the airtight hood case exhibits a notably higher negative pressure amplitude on the train body compared to the PMH cases. This observation underscores the effectiveness of PMH in mitigating the effects of expansion waves induced by the train tail entering the PMH I region.

Figure 17(a) offers additional perspectives on how porosity affects the initial wavefront, showcasing instantaneous pressure fields captured at three distinct moments on the $z = 0.5H$ plane. The wavefront amplitude in the PMH I region gradually decreases as the porosity increases, which is consistent with the results shown in Fig. 11(a). Importantly, the expansion wave generated by the tail train entering the PMH I region is significantly suppressed observed at $tV_t/H = 36$. The suppression function of PMH on expansion waves helps to reduce the transient pressure amplitude acting on the train within a short period, thereby mitigating pressure fluctuations inside the train and enhancing ear comfort for passengers.[53] Figure 17(b) illustrates the propagation and dissipation of the initial wavefront within the PMH II region. Across all cases, the MPW initially propagates downstream in an ellipsoid shape, subsequently transitioning into a spherical form.[54] The MPW for the airtight hood case begins to radiate only at the exit of PMH II. However, for cases where PMH is installed at the tunnel's end, the initial wavefront leaks pressure outwards within the PMH II region, radiating its primary energy (i.e., MPW) at the exit of PMH II. An intriguing observation is that the wavefront propagation velocity within the PMH II region consistently exceeds that of the pressure outside, with this disparity becoming more evident as porosity diminishes.

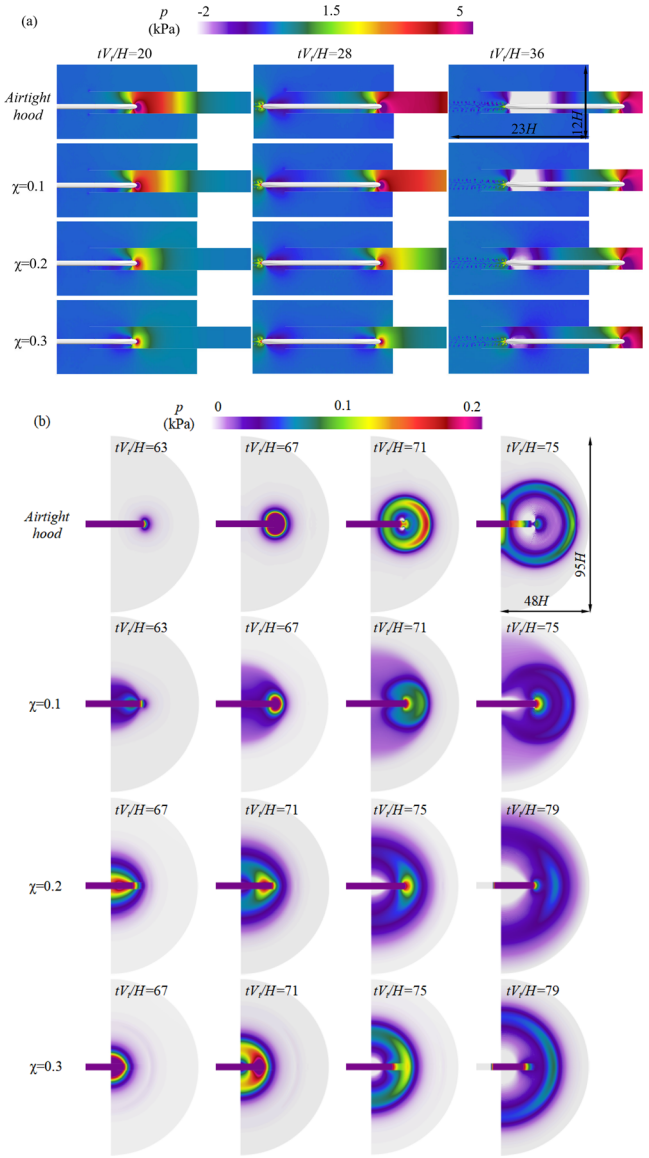

FIG. 17. Horizontal pressure evolution for the $z = 0.5H$ plane: (a) the evolution of the initial wavefront and (b) the evolution of MPW radiation.

The data presented in Fig. 17(b) indicates that the case with $\chi = 0.2$ can uniformly release pressure within the PMH II region while achieving optimal mitigation of the MPW.

B. Influence of PMH length

Based on the preceding investigations, the porosity of the PMH in this section is adopted as 0.2, with a thickness of 3.5 mm. The impact of PMH length on the initial wavefront properties is illustrated in Fig. 18. The alteration in PMH length will inevitably influence the distribution pattern of wavefront amplitude along the tunnel.[55] The impact of PMH length on wavefront amplitude is minimal in the PMH I zone and the tunnel, with notable variations primarily evident within the PMH II zone. A rapid decrease in wavefront amplitude occurs at the $x/L_{tu} = 1$ position. The wavefront amplitude at the exit of PMH II decreases significantly with the increasing PMH length. The wavefront gradient magnitude decreases overall as the length of PMH increases. Compared to the $L_{PMH} = 2.5$ m case, the wavefront gradient magnitudes at the PMH II exit for $L_{PMH} = 3.75$ m and $L_{PMH} = 5$ m cases decrease by 39.6% and 63.8%, respectively. Thus, extending the PMH in the exit zone can enhance MPW mitigation by facilitating sustained and uniform pressure relief along the wall's normal direction. The temporal wavefront and its gradient at the location $x/L_{tu} = 0.2$ are illustrated in Figs. 18(c) and 18(d), respectively. Increasing the PMH length primarily reduces the wavefront gradient magnitude by extending the rise time of the wavefront.

Figures 19(a) and 19(b) illustrate the effect of PMH length on MPW at positions of $x_M = 1$ m and $x_M = 2.5$ m, respectively. As the PMH increases, the timing of the peak MPW occurrence at a fixed location correspondingly delays. Compared to the prototype case, the MPW amplitudes at $x_M = 1$ m and $x_M = 2.5$ m in the $L_{PMH} = 5$ m scenario decrease by 83.5% and 75.9%, respectively. The distribution of MPW amplitudes along the streamwise direction under different PMH lengths is displayed in Fig. 19(c). The functional relationship between MPW amplitude and the distance x_M for three cases is presented in Fig. 19(c), all exhibiting a power-law relationship with a high degree of fit. The effect of PMH length on the unweighted SPL of MPW is demonstrated in Fig. 20. The unweighted SPLs at the two locations under the $L_{PMH} = 5$ m case have fallen below the hearing threshold within the frequency range of 20–40 Hz. Although some SPLs in this case reach the 25-phon level, they already belong to a relatively low audible noise range. Combining the data from Fig. 14(c), both the C-weighted sound peak levels for the $L_{PMH} = 3.75$ m and $L_{PMH} = 5$ m cases can fall below the 115 dB(C) requirement outlined in European directive 2003/10/EC.

C. Influence of PMH thickness

Based on Eq. (9), the pressure drop across the PMH region during normal flow increases with the thickness of PMH. Taking a porosity of 0.2 and a length of 75 m as the reference, Fig. 21 illustrates how variations in PMH thickness impact MPW characteristics. The thickness alters the MPW waveform, particularly exhibiting a hump-shaped pattern in the case of $h = 10$ mm. This phenomenon exhibits a resemblance to the MPW waveform observed in the $\chi = 0.1$ scenario depicted in Fig. 13(b). When a substantial pressure drop occurs across the porous media zone, the train's ingress into both PMH I and the tunnel entrance triggers initial wavefronts with varying strengths. The cumulative effect of these two wavefronts eventually shapes the MPW into a distinctive hump-like form. Increasing the PMH thickness has a minor impact on the MPW amplitude, slightly enhancing the amplitude before x_M=1m and diminishing it thereafter. The alterations in MPW contours are reflected in Fig. 22, showcasing distinct behaviors below 20 Hz. Specifically, the SPL curves for $h = 7$ mm and $h = 10$ mm cases exhibit fluctuations, whereas the $h = 3.5$ mm case presents a smoother decline in SPL below 20 Hz. Regarding the SPL curves exceeding 20 Hz, the disparities between the three cases are minimal.

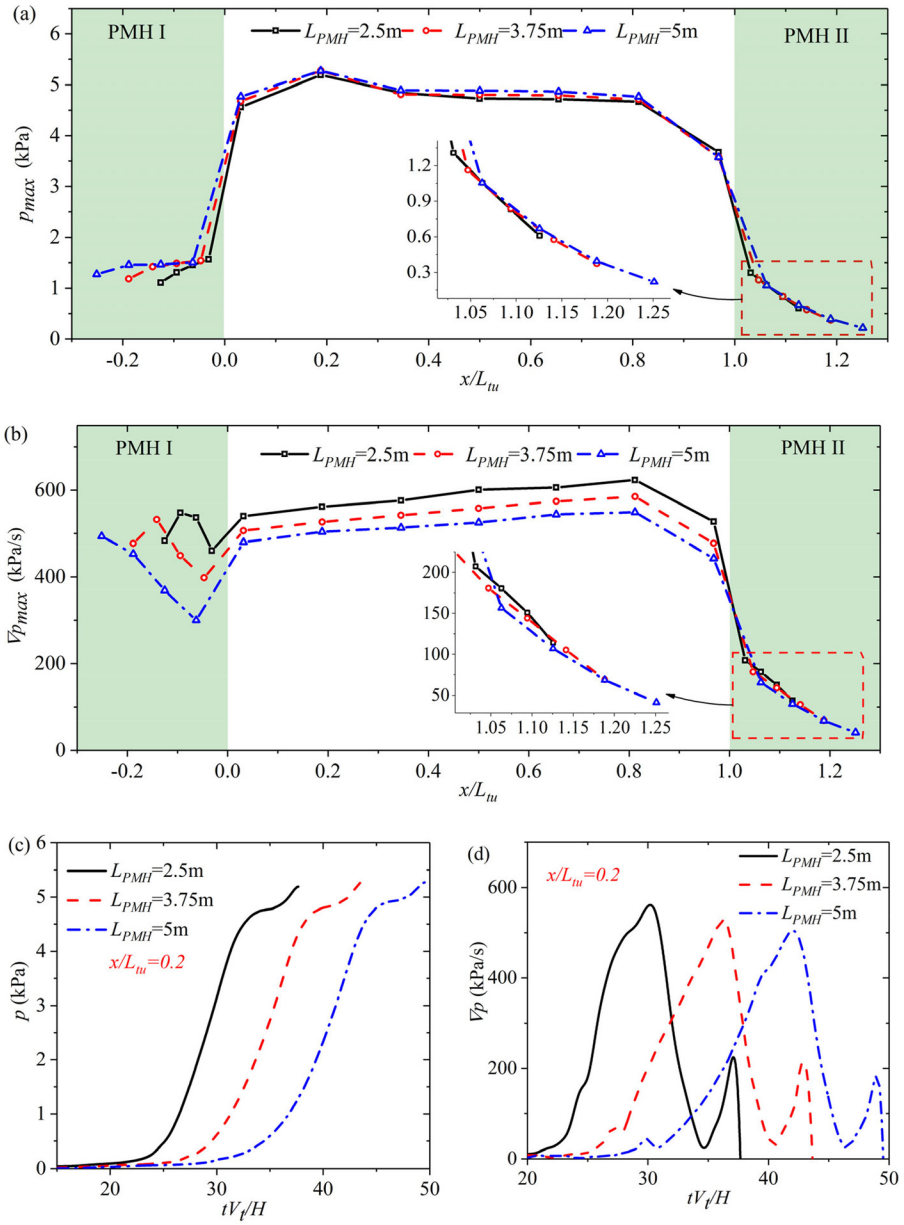

FIG. 18. Influence of PMH length on the wavefront characteristics: (a) distribution of the wavefront amplitude, (b) distribution of the wavefront gradient amplitude, (c) the wavefront evolution at $x/L_{tu} = 0.2$ location, and (d) the wavefront gradient evolution at $x/L_{tu} = 0.2$ location.

D. Discussion

1. Aerodynamic forces of the train

While the primary focus of this paper is on elucidating the mitigating effects of PMH on tunnel exit sonic booms, it is imperative to discuss the consequences of PMH on train aerodynamics forces[56] and surface pressure distributions.[57] Figures 23(a) and 23(b) compare the aerodynamic drag acting on the train between the airtight hood and the $\chi = 0.2$ case (with a length of 3.75 m and a thickness of 3.5 mm). The aerodynamic drag of the train is primarily influenced by the portal effect as the train enters and exits the tunnel, as well as the pressure waves within the tunnel.[58] Within the time interval of $15 < tV_t/H < 60$, the PMH I zone mitigates the expansion wave generated by the train's rear entering the tunnel. Typically, this expansion wave would contribute to an increase in train drag, but in the $\chi = 0.2$ scenario, the negative peak of drag (Fx_{min}) is diminished. Furthermore, the fluctuation in drag experienced by the train as it passes through the PMH II region is also reduced in the $\chi = 0.2$ case. Compared to the airtight hood, the Fx_{min} reductions for the head, middle, and tail cars in the $\chi = 0.2$ case are 5.2%, 8.8%, and 16.4%, respectively. The lateral force on the train primarily stems from the asymmetric flow field on its lateral sides, particularly evident during the train's entry and exit from the tunnel [see Fig. 23(c)]. Figures 16 and 17(a) demonstrate that PMH can reduce the turbulence intensity of the wake flow when the

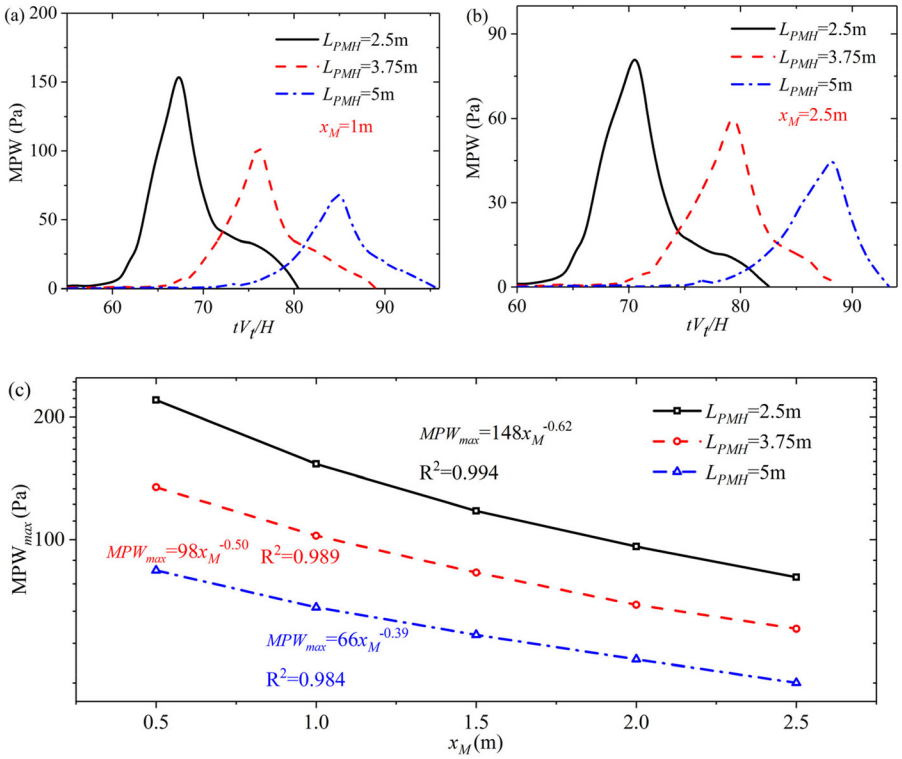

FIG. 19. Influence of PMH length on the MPW characteristics: (a) temporal MPW under different porosity at $x_M = 1$ m location, (b) temporal MPW under different porosity at $x_M = 2.5$ m location, and (c) the distribution of MPW amplitude along the streamwise direction under different PMH lengths.

train enters and exits the tunnel and form a more symmetrical flow field in the spanwise direction of the train. Compared to the airtight hood, the peak-to-peak lateral force (ΔFy) for the head, middle, and tail cars in the $\chi = 0.2$ case is reduced by 30.0%, 36.6%, and 40.4%, respectively.

2. Pressure fluctuation of the train

Figure 24 presents a comparative analysis of the pressure evolution at the mid-body of the train between the airtight hood and the $\chi = 0.2$ case (with a length of 3.75 m and a thickness of 3.5 mm). Within the time interval of $30 < tV_t/H < 60$, the expansion wave generated by the tail train entering the tunnel in the $\chi = 0.2$ case is delayed, and the pressure gradient within this period is smaller. During the time interval of $75 < tV_t/H < 90$, the initial compression wave generated by the head train entering the tunnel is reflected as an expansion wave upon reaching the tunnel exit and interacts with the train, resulting in a drop in the tap pressure. The absolute value of p_{min} during this time interval is smaller in the $\chi = 0.2$ case, indicating that the intensity of the expansion wave is significantly weakened when it is reflected in the PMH II exit. Compared to the airtight hood, the peak-to-peak pressure (Δp) at the streamwise train surfaces in the $\chi = 0.2$ case is reduced by 8.1%–14.5%. The reductions in both the peak-to-peak pressure and pressure gradient on the train surface indicate that the PMH can enhance the comfort level for passengers' ears.

3. Remission rate of MPW

The current mitigation solutions for the tunnel sonic boom involve an enlarged cross-section hood, oblique hood, vented hood,

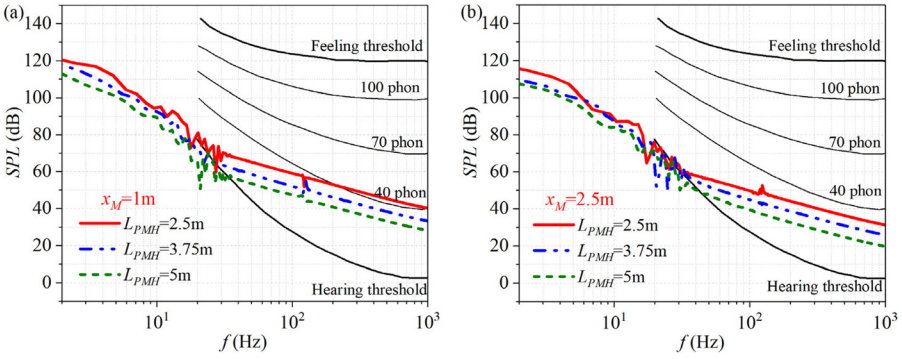

FIG. 20. Influence of PMH length on the MPW SPL: (a) unweighted SPL at $x_M = 1$ m position referenced to equal-loudness-level contours and (b) unweighted SPL at $x_M = 2.5$ m position referenced to equal-loudness-level contours.

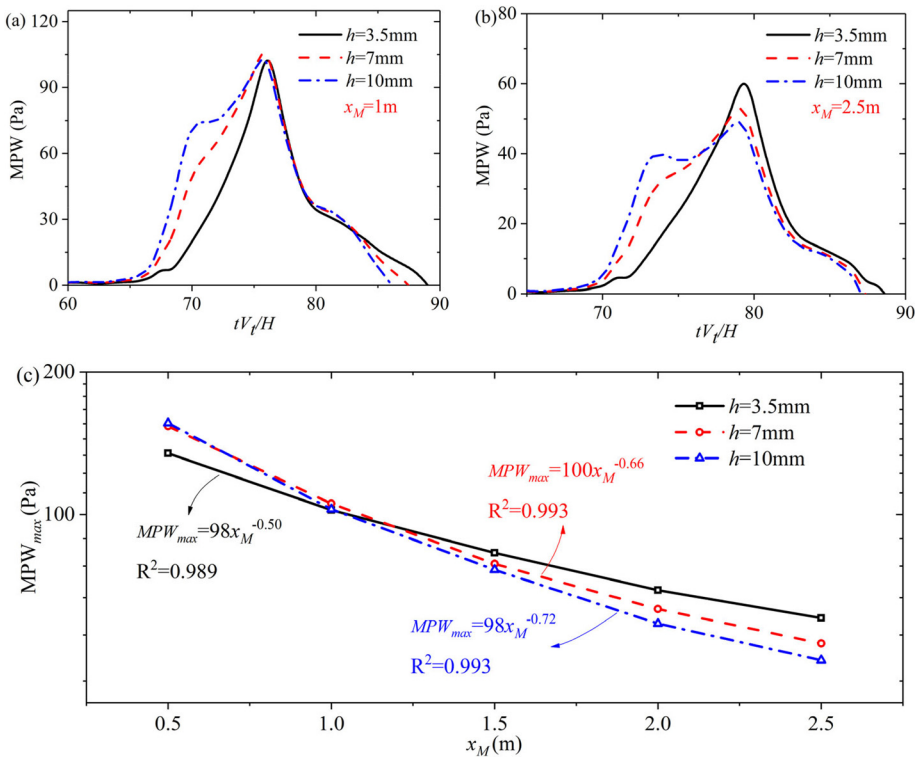

FIG. 21. Influence of PMH thickness on the MPW characteristics: (a) temporal MPW under different porosity at $x_M = 1$ m location, (b) temporal MPW under different porosity at $x_M = 2.5$ m location, and (c) the distribution of MPW amplitude along the streamwise direction under different PMH thickness.

and some bio-inspired hoods. Their effectiveness lies in their geometrical shapes, with two key parameters being the length and the area (S_{hood}) of the hood. Hence, Fig. 25 showcases a comparative analysis of MPW mitigation rates between various typical hoods and the current study, all measuring 20 m from the tunnel exit. These representative hoods include the biomimetic shark gill hood proposed by Kim *et al.*[21] and Lin *et al.*,[22] a vented hood with a decreasing open ratio[28] and an arch lattice-shell hood with an enlarged cross section[27] studied by Zhang *et al.*, and a combined buffer hood explored by Li *et al.*[22] Only Zhang *et al.*[27,28] and the current work have installed hoods of equal length at both ends of the tunnel. Additionally, only Lin *et al.*[22] and the current work have a ratio of hood area to tunnel area (S_{tu}) of 1. Figure 25 shows that the vented hood with a decreasing open ratio proposed by Zhang *et al.*[28] can reduce MPW by 86.7%, followed by our work with a reduction ratio of 83.5% (with a full-scaled length $L_{PMH} = 100$ m, porosity $\chi = 0.2$, and thickness $h = 3.5$ mm). The hood studied by Zhang *et al.*[28] has an area twice that of the tunnel, whereas the hood in current research has an area equal to that of the tunnel. Therefore, the above results demonstrate the feasibility and superiority of the porous media hood in mitigating the sonic boom emitted from the maglev tunnel portals.

IV. CONCLUSION

This study systematically investigates the impact of PMH on the coupled train/tunnel aerodynamic effects at 600 km/h. To solve the simulation model, the IDDES turbulence model based on SST k–ω and overset grid technology has been employed. The validity of the numerical method has been confirmed through moving-model experiments with silencers installed at the tunnel exit, as well as experimental data from 600 km/h maglev moving-model experiments. The porosity,

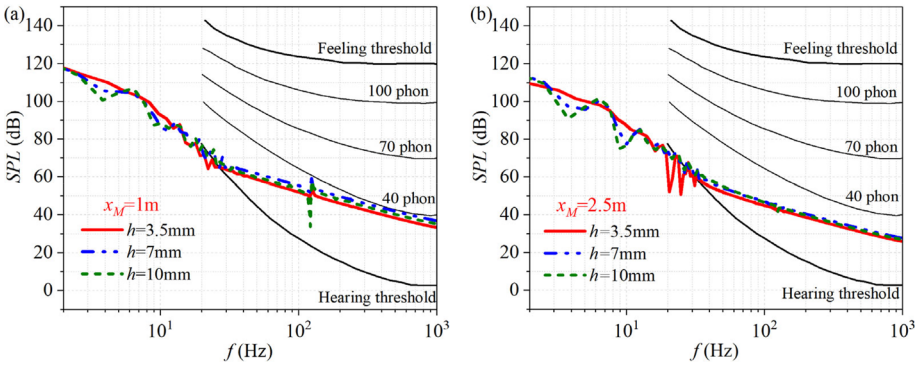

FIG. 22. Influence of PMH thickness on the MPW SPL: (a) unweighted SPL at $x_M = 1$ m position referenced to equal-loudness-level contours and (b) unweighted SPL at $x_M = 2.5$ m position referenced to equal-loudness-level contours.

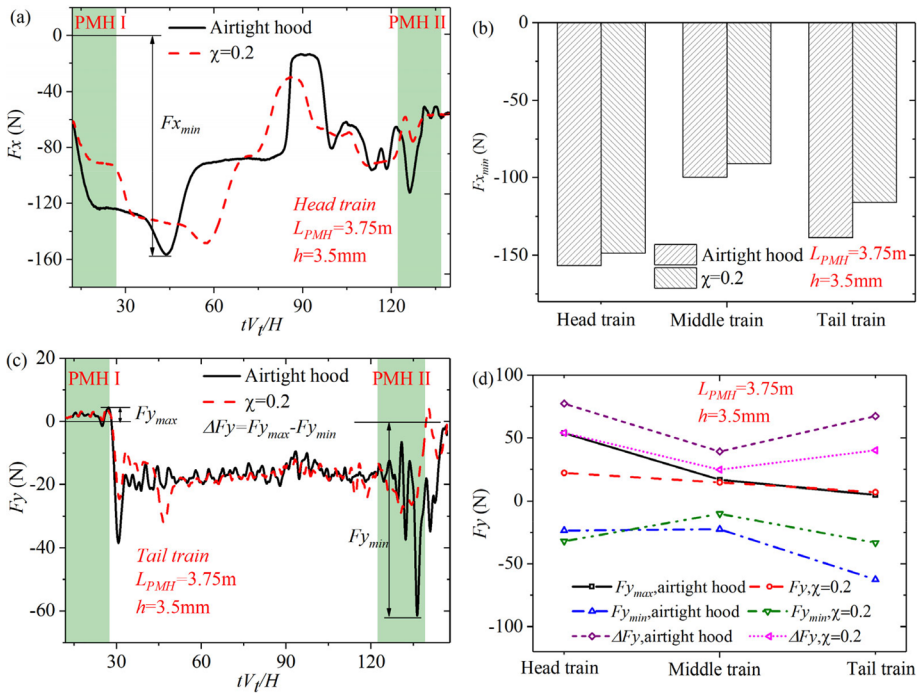

FIG. 23. Influence of PMH on the aerodynamic forces of the train: (a) comparison of temporal train drag force between the airtight hood and PMH, (b) mitigation analysis of drag force amplitude by PMH, (c) comparison of temporal train lateral force between the airtight hood and PMH, and (d) mitigation analysis of lateral force amplitude by PMH.

length, thickness, and MPW mitigation efficiency of PMH have been comprehensively analyzed, and the optimal parameters have been determined. The main research conclusions are outlined as follows:

(1) A porous media model has been developed and validated using data from moving-model experiments. The errors in MPW amplitude between experiments and simulations across four train speeds are all within 3.9%, confirming the reliability of the current porous media model and IDDES simulation methodology.
(2) The pressure drop across PMH is not constant under transient wavefront conditions. The inlet PMH relieves the initial wavefront gradient by dissipating pressure, while the outlet PMH attenuates the amplitude of the MPW in front, albeit at the expense of increased radiation within its streamwise domain.
(3) The porosity of 0.2 optimizes the transition from the ventilated zone to the airtight tunnel environment for streamlined trains. Increasing the PMH length provides a sustained mitigation effect on MPW, while the impact of PMH thickness is comparatively minor. When PMH has a porosity of 0.2, a length of 5 m, and a thickness of 3.5 mm, the MPW amplitude at the $x_M = 1$ m location is reduced by 83.5%. The C-weighted sound peak level at the specified location falls below 115 dB(C).
(4) PMH reduces the reflection intensity of initial compression and expansion waves at tunnel ends, thereby mitigating the peaks and changing rates in aerodynamic forces and surface pressures on trains. By regulating the flow field balance on both sides of the train during tunnel entry, PMH minimizes the fluctuations of the train's lateral force. This demonstrates PMH's potential to enhance passengers' auditory comfort during tunnel traversal and mitigate train sway issues.

The current PMH adopts a cross-sectional shape that is equal to that of the tunnel. Enlarged cross sections, flare designs, and oblique

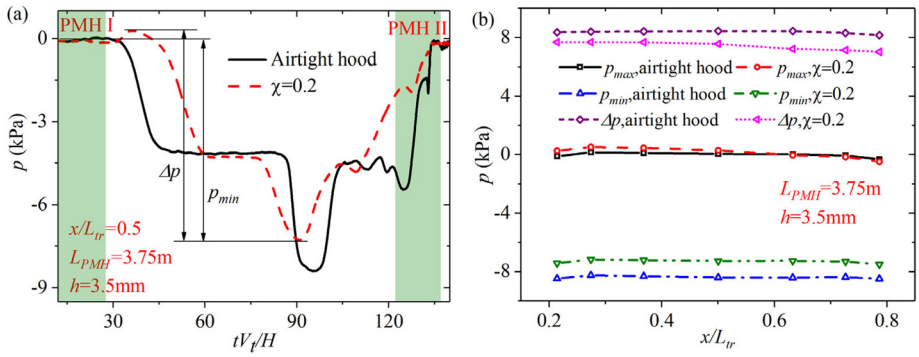

FIG. 24. Influence of PMH on the pressure fluctuation of the train: (a) comparison of temporal train surface pressure between the airtight hood and $\chi = 0.2$ case and (b) mitigation analysis of pressure amplitude of the train surface by $\chi = 0.2$ case.

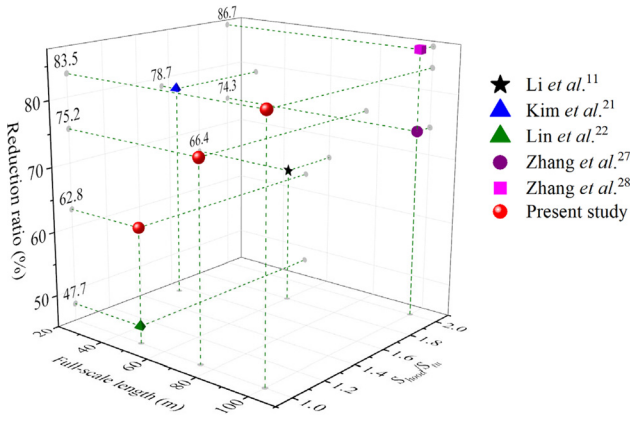

FIG. 25. Comprehensive analysis of the mitigation effect of hood on MPW considering two factors hood length and hood area. The reduction ratios are calculated from the data of the current study and previous literature.

angles can all be incorporated into the current shape to further enhance its MPW mitigation effects. The mechanical performance response and fatigue strength evaluation of PMH under aerodynamic forces are also worthy of investigation. Additionally, porous media materials can be used as a substitute physical model for ballast, thus solving the difficult problem of complex and difficult-to-calculate three-dimensional structures of ballast. In the future, we will investigate the impact of installing porous media coatings on the tunnel wall on the train/tunnel coupling aerodynamic effects. The mechanisms of porous media coatings, as substitutes for ballast, in mitigating wavefront gradients and MPW will be analyzed. Furthermore, the porous media model can also be utilized to explore the flow field characteristics under the train, providing further insights into the causes of ballast splash.

ACKNOWLEDGMENTS

The authors acknowledge the computational resources provided by the High-Performance Computing Center of Central South University, China. This work was supported by the National Key R & D program of China (Grant Nos. 2020YFA0710903 and 2023YFB4302502-02), the Open Foundation of National Engineering Research Center of High-speed Railway Construction Technology (Grant No. HSR202212), and the National Natural Science Foundation of China (Grant No. 52372369).

AUTHOR DECLARATIONS

Conflict of Interest

The authors have no conflicts to disclose.

Author Contributions

Kai-Wen Wang: Conceptualization (equal); Data curation (equal); Formal analysis (equal); Software (equal); Validation (equal); Visualization (equal); Writing – original draft (equal). **Guang Chen:** Conceptualization (equal); Formal analysis (equal); Investigation (equal); Writing – review & editing (equal). **Chih-Yung Wen:** Conceptualization (equal); Formal analysis (equal); Investigation (equal); Writing – review & editing (equal). **Xiao-Hui Xiong:** Conceptualization (equal); Funding acquisition (equal); Supervision (equal); Validation (equal). **Xi-Feng Liang:** Conceptualization (equal); Funding acquisition (equal). **Lei Zhang:** Data curation (equal); Investigation (equal).

DATA AVAILABILITY

The data that support the findings of this study are available from the corresponding author upon reasonable request.

REFERENCES

[1]Z. Chen, Z. Guo, Y. Ni, T. Liu, and J. Zhang, "A suction method to mitigate pressure waves induced by high-speed maglev trains passing through tunnels," Sustainable Cities Soc. **96**(5), 104682 (2023).
[2]Y. Shi, W. Ma, M. Li, and Z. Xu, "Research on dynamics of a new high-speed maglev vehicle," Veh. Syst. Dyn. **60**(3), 721–742 (2022).
[3]F. Dong, Z. Huang, L. Hao, X. Xu, Z. Jin, and N. Shao, "An on-board 2G HTS magnets system with cooling-power-free and persistent-current operation for ultrahigh speed superconducting maglevs," Sci. Rep. **9**(1), 11844 (2019).
[4]P. Schmid, G. Schneider, F. Dignath, X. Liang, and P. Eberhard, "Static and dynamic modeling of the electromagnets of the maglev vehicle transrapid," IEEE Trans. Magn. **57**(2), 1 (2021).
[5]S. Han, J. Zhang, X. H. Xiong, P. Ji, L. Zhang, J. Sheridan, and G. J. Gao, "Influence of high-speed maglev train speed on tunnel aerodynamic effects," Build. Environ. **223**(8), 109460 (2022).
[6]S. Saito, "Alleviation of micro-pressure waves radiated from tunnel hoods," Tunnelling Underground Space Technol. **147**(10), 105703 (2024).
[7]B. Auvity and M. Bellenoue, "Effects of an opening on pressure wave propagation in a tube," J. Fluid Mech. **538**, 269–289 (2005).
[8]J. Niu, Y. Wang, H. Yao, and Y. Huang, "Numerical investigation on application of train body airflow diversion device to suppress pressure waves in railway high-speed train/tunnel system," Int. J. Rail Transp. **11**(4), 490–507 (2023).
[9]J. M. Rivero, E. González-Martínez, and M. Rodríguez-Fernández, "A methodology for the prediction of the sonic boom in tunnels of high-speed trains," J. Sound Vib. **446**, 37–56 (2019).
[10]K. Wang, X. Xiong, C. Wen, G. Chen, X. Liang, H. Huang, and J. Wang, "Formation and propagation characteristics of a weak shock wave in maglev tube," Phys. Fluids **36**(3), 036120 (2024).
[11]G. Li, X. Ye, E. Deng, W. Yang, Y. Ni, H. He, and W. Ao, "Aerodynamic mechanism of a combined buffer hood for mitigating micro-pressure waves at the 400 km/h high-speed railway tunnel portal," Phys. Fluids **35**(12), 126106 (2023).
[12]X. Xiang, L. Xue, B. Wang, and W. Zou, "Mechanism and capability of ventilation openings for alleviating micro-pressure waves emitted from high-speed railway tunnels," Build. Environ. **132**(1), 245–254 (2018).
[13]A. E. Vardy and J. M. B. Brown, "Influence of ballast on wave steepening in tunnels," J. Sound Vib. **238**(4), 595–615 (2000).
[14]J. A. Tebbutt, M. Vahdati, D. Carolan, and J. P. Dear, "Numerical investigation on an array of Helmholtz resonators for the reduction of micro-pressure waves in modern and future high-speed rail tunnel systems," J. Sound Vib. **400**, 606–625 (2017).
[15]H. Wang, A. E. Vardy, and H. Bi, "Characteristics of pressure waves radiated from tunnel portals in cuttings," J. Sound Vib. **521**(10), 116664 (2022).
[16]H. Wang, A. E. Vardy, and D. Pokrajac, "Pressure radiation from a perforated duct exit region," J. Sound Vib. **351**(5), 29–42 (2015).
[17]M. S. Howe, M. Iida, T. Fukuda, and T. Maeda, "Theoretical and experimental investigation of the compression wave generated by a train entering a tunnel with a flared portal," J. Fluid Mech. **425**, 111–132 (2000).
[18]L. Zhang, M. Yang, X. Liang, and J. Zhang, "Oblique tunnel portal effects on train and tunnel aerodynamics based on moving model tests," J. Wind Eng. Ind. Aerodyn. **167**(8), 128–139 (2017).

[19]T. Miyachi and T. Fukuda, "Model experiments on area optimization of multiple openings of tunnel hoods to reduce micro-pressure waves," Tunnelling Underground Space Technol. **115**(8), 103996 (2021).
[20]T. Lin, M. Yang, L. Zhang, T. Wang, D. Liu, Y. Tao, and S. Zhong, "Influence of the suspension gap on the wake characteristics of a 600 km/h superconducting maglev train," Phys. Fluids **36**(2), 026121 (2024).
[21]D. H. Kim, S. Y. Cheol, R. S. Iyer, and H. D. Kim, "A newly designed entrance hood to reduce the micro pressure wave emitted from the exit of high-speed railway tunnel," Tunnelling Underground Space Technol. **108**(10), 103728 (2021).
[22]T. Lin, M. Yang, L. Zhang, T. Wang, and S. Zhong, "Influence of bionics shark gills tunnel portal on the micro-pressure wave at the tunnel exit," Tunnelling Underground Space Technol. **144**, 105542 (2024).
[23]T. Fukuda, S. Nakamura, T. Miyachi, S. Saito, N. Kimura, and M. Matsunuma, "Influence of ballast quantity on compression wavefront steepening in railway tunnels," Proc. Inst. Mech. Eng., Part F **234**(6), 607–615 (2020).
[24]F. Liu, A. E. Vardy, and D. Pokrajac, "Influence of air chambers on wavefront steepening in railway tunnels," Tunnelling Underground Space Technol. **117**(8), 104120 (2021).
[25]R. S. Iyer, D. H. Kim, and H. D. Kim, "Effect of air chambers on the compression wave propagating along a high-speed railway tunnel," J. Mech. Sci. Technol. **37**(2), 793–805 (2023).
[26]N. Sugimoto, M. Masuda, K. Yamashita, and H. Horimoto, "Verification of acoustic solitary waves," J. Fluid Mech. **504**, 271–299 (2004).
[27]J. Zhang, Y. Wang, S. Han, F. Wang, and G. Gao, "A novel arch lattice-shell of enlarged cross-section hoods for micro-pressure wave mitigation at exit of maglev tunnels," Tunnelling Underground Space Technol. **132**(7), 104859 (2023).
[28]J. Zhang, B. Guo, Y. Wang, S. Han, X. Xiong, S. Krajnović, and G. Gao, "A novel vented tunnel hood with decreasing open ratio to mitigate micro-pressure wave emitted at high-speed maglev tunnel exit," J. Wind Eng. Ind. Aerodyn. **240**(5), 105459 (2023).
[29]K. Ootsuta, K. Matsuoka, A. Sasoh, and K. Takayama, "Application of sound-absorbent plastic to weak-shock-wave attenuators," Rev. Sci. Instrum. **69**(4), 1724–1729 (1998).
[30]M. E. Rosti, L. Brandt, and A. Pinelli, "Turbulent channel flow over an anisotropic porous wall—Drag increase and reduction," J. Fluid Mech. **842**, 381–394 (2018).
[31]W. P. Breugem, B. J. Boersma, and R. E. Uittenbogaard, "The influence of wall permeability on turbulent channel flow," J. Fluid Mech. **562**, 35–72 (2006).
[32]P. Zhao, Z. Zhao, and C. Yang, "Investigation of the orifice flow of over-the-rotor liner and its interaction with the rotor flow field," Phys. Fluids **35**(10), 107144 (2023).
[33]D. Sun, J. Li, R. Xu, X. Dong, D. Zhao, and X. Sun, "Effects of the foam metal casing treatment on aerodynamic stability and aerocoustic noise in an axial flow compressor," Aerosp. Sci. Technol. **115**, 106793 (2021).
[34]H. Liu, J. Wei, and Z. Qu, "Prediction of aerodynamic noise reduction by using open-cell metal foam," J. Sound Vib. **331**(7), 1483–1497 (2012).
[35]M. Yang, S. Zhong, L. Zhang, B. Qian, T. Wang, D. Zhou, and F. Wu, "600 Km/H moving model rig for high-speed train aerodynamics," J. Wind Eng. Ind. Aerodyn. **227**(5), 105063 (2022).
[36]T. Miyachi, K. Kikuchi, and M. Hieke, "Multistep train nose for reducing micro-pressure waves," J. Sound Vib. **520**(11), 116665 (2022).
[37]CEN European Standard, "Railway applications—Aerodynamics. Part 4: Requirements and test procedures for aerodynamics on open track," TSI/EN 14067–4, CEN European Standard, 2013.
[38]T. Dong, G. Minelli, J. Wang, X. Liang, and S. Krajnović, "Numerical investigation of a high-speed train underbody flows: Studying flow structures through large-eddy simulation and assessment of steady and unsteady Reynolds-averaged Navier–Stokes and improved delayed detached eddy simulation performance," Phys. Fluids **34**, 015126 (2022).
[39]K. Wang, X. Xiong, T. Dong, and G. Chen, "A two-dimensional revolving-axi-symmetric model for assessing the wave effects inside the railway tunnel," J. Wind Eng. Ind. Aerodyn. **248**(9), 105716 (2024).
[40]M. L. Shur, P. R. Spalart, M. K. Strelets, and A. K. Travin, "A hybrid RANS-LES approach with delayed-DES and wall-modelled LES capabilities," Int. J. Heat Fluid Flow **29**(6), 1638–1649 (2008).
[41]Siemens, "Simcenter STAR-CCM+® documentation," 1–11930 (2023).
[42]H. Huang and J. Ayoub, "Applicability of the Forchheimer equation for non-Darcy flow in porous media," SPE J. **13**(1), 112–122 (2008).
[43]S. B. Pope, *A Perspective on Turbulence Modeling*, ICASE/LaRC Interdisciplinary Series in Science and Engineering (Springer, Netherlands, 1999).
[44]I. B. Celik, Z. N. Cehreli, and I. Yavuz, "Index of resolution quality for large eddy simulations," J. Fluids Eng. **127**(5), 949–958 (2005).
[45]C. Y. Li, Z. Chen, T. K. T. Tse, A. U. Weerasuriya, X. Zhang, Y. Fu, and X. Lin, "A parametric and feasibility study for data sampling of the dynamic mode decomposition: Range, resolution, and universal convergence states," Nonlinear Dyn. **107**(4), 3683–3707 (2022).
[46]K. Takayama, A. Sasoh, O. Onodera, R. Kaneko, and Y. Matsui, "Experimental investigation on tunnel sonic boom," Shock Waves **5**(3), 127–138 (1995).
[47]X. Tan, L. Jiang, X. Li, Y. Li, and K. Zhang, "A complex model for the permeability and porosity of porous media," Chem. Eng. Sci. **172**, 230–238 (2017).
[48]A. Aydın, T. Engin, H. Yasar, A. Yeter, and A. H. Perut, "Computational fluid dynamics analysis of a vehicle radiator using porous media approach," Heat Transfer Eng. **42**(11), 904–916 (2021).
[49]R. Yamashita and H. Ishikawa, "A semi-adapted space marching method for fast sonic boom prediction," J. Comput. Phys. **487**, 112170 (2023).
[50]Y. Suzuki and H. Takeshima, "Equal-loudness-level contours for pure tones," J. Acoust. Soc. Am. **116**(2), 918–933 (2004).
[51]The European Parliament and of the Council, "Minimum health and safety requirements regarding the exposure of workers to the risks arising from physical agents (noise)," European Directive 2003/10/EC, 2003.
[52]T. Gilbert, C. J. Baker, and A. Quinn, "Gusts caused by high-speed trains in confined spaces and tunnels," J. Wind Eng. Ind. Aerodyn. **121**, 39–48 (2013).
[53]P. Xie, Y. Peng, T. Wang, and H. Zhang, "Risks of ear complaints of passengers and drivers while trains are passing through tunnels at high speed: A numerical simulation and experimental study," Int. J. Environ. Res. Public Health **16**(7), 1283 (2019).
[54]G. Zhang, T. H. Kim, D. H. Kim, and H. D. Kim, "Prediction of micro-pressure waves generated at the exit of a model train tunnel," J. Wind Eng. Ind. Aerodyn. **183**(8), 127–139 (2018).
[55]M. William-Louis and C. Tournier, "A wave signature based method for the prediction of pressure transients in railway tunnels," J. Wind Eng. Ind. Aerodyn. **93**(6), 521–531 (2005).
[56]J. K. Choi and K. H. Kim, "Effects of nose shape and tunnel cross-sectional area on aerodynamic drag of train traveling in tunnels," Tunnelling Underground Space Technol. **41**(1), 62–73 (2014).
[57]K. Jin, L. Zhang, X. Li, L. Li, J. Chen, J. Wang, and J. Niu, "Effect of characteristic parameters of air-bleeding/blowing interface on tunnel pressure waves in streamlined regions of high-speed trains: A numerical simulation study," Sustainable Cities Soc. **102**(1), 105222 (2024).
[58]H. Kwon, Y. Jin, W. Lee, and H. Kang, "The feasibility of adapting air compressor to a high-speed train to attenuate the aerodynamic problems in tunnel," Int. J. Aeronaut. Space Sci. **21**(3), 638–646 (2020).